Lithos 296–299 (2018) 245–264

Contents lists available at ScienceDirect

Lithos

journal homepage: www.elsevier.com/locate/lithos

Textural and chemical evolution of pyroxene during hydration and deformation: A consequence of retrograde metamorphism

Stephen Centrella [a,*], Andrew Putnis [a,b], Pierre Lanari [c], Håkon Austrheim [d]

[a] Institut für Mineralogie, University of Münster, D-48149 Münster, Germany
[b] The Institute for Geoscience Research (TIGeR), Curtin University, Perth 6102, Australia
[c] Institute of Geological Sciences, University of Bern, CH3012 Bern, Switzerland
[d] PGP, Department of Geosciences, University of Oslo, N-0316, Norway

ARTICLE INFO

Article history:
Received 18 April 2017
Accepted 1 November 2017
Available online 23 November 2017

ABSTRACT

Centimetre-sized grains of Al-rich clinopyroxene within the granulitic anorthosites of the Bergen Arcs, W-Norway undergo deformation by faults and micro-shear zones (kinks) along which fluid has been introduced. The clinopyroxene (11 wt% Al_2O_3) reacts to the deformation and hydration in two different ways: reaction to garnet ($Alm_{41}Prp_{32}Grs_{21}$) plus a less aluminous pyroxene (3 wt% Al_2O_3) along kinks and the replacement of the Al-rich clinopyroxene by chlorite along cleavage planes. These reactions only take place in the hydrated part of a hand specimen that is separated from dry, unreacted granulite by a sharp interface that defines the limit of hydration. We use electron probe microanalysis (EPMA) and X-Ray mapping together with electron backscatter diffraction (EBSD) mapping to investigate the spatial and possible temporal relationships between these two parageneses. Gresens' analysis (Gresens, 1967) has been used to determine the mass balance and the local volume changes associated with the two reactions. The reaction to garnet + low-Al clinopyroxene induces a loss in volume of the solid phases whereas the chlorite formation gains volume. Strain variations result in local variation in undulose extinction in the parent clinopyroxene. EBSD results suggest that the density-increasing reaction to garnet + low-Al clinopyroxene takes place where the strain is highest whereas the density-decreasing reaction to chlorite forms away from shear zones where EBSD shows no significant strain. Modelling of phase equilibria suggest that the thermodynamic pressure of the assemblage within the shear zones is >6 kbar higher than the pressure conditions for the whole rock for the same range of temperature (~650 °C). This result suggests that the stress redistribution within a rock may play a role in determining the reactions that take place during retrograde metamorphism.

© 2017 Elsevier B.V. All rights reserved.

1. Introduction

The partial hydration of a dry granulite-facies rock from the lower crust during orogenesis and retrograde metamorphism is a fundamental process of re-equilibration of a rock with an initially low permeability. Understanding the interaction between fluid infiltration, mineral reactions and deformation in such a context is an important goal in metamorphic petrology and has been the subject of many studies related to the mechanism of fluid transport, the role of deformation in initiating and driving fluid flow and the close relationship between mineral reaction, strength of a rock and deformation mechanisms (Beach and Fyfe, 1972; Boundy et al., 1992; Fukuda et al., 2012; Fyfe et al., 1978; Gratier et al., 2013; Marsh et al., 2009; Mukai et al., 2014; Svahnberg and Piazolo, 2010, 2013; Wawrzenitz et al., 2012; Wintsch and Yeh, 2013).

Metamorphic reactions associated with fluid infiltration and hydration influence rock strength by forming new, softer, less dense minerals and/or by reducing the grain size (Fitz Gerald and Stünitz, 1993; de Bresser et al., 2001; de Ronde et al., 2004, 2005; Holyoke and Tullis, 2006; Pearce et al., 2011). Moreover, the fluid phase present during metamorphism (Carmichael, 1969; Philipotts and Ague, 2013; Putnis and Austrheim, 2010) may control whether dislocation creep or dissolution-precipitation creep is the dominant deformation mechanism for a specific range of pressure and temperature (Heidelbach et al., 2000; Karato, 1988; Menegon et al., 2008; Mukai et al., 2014; Rutter et al., 1994).

Hydration reactions can also involve a local density change of the solid system that may generate a local stress, the magnitude depending on how open the system is to mass transport (Ague, 1991, 1994; Centrella et al., 2015, 2016; Jamtveit et al., 2000, 2008; Jamtveit and Hammer, 2012; Kelemen and Hirth, 2012; Wheeler, 1987). Local variations in mineral assemblages have been interpreted to result from reaction driven grain-scale pressure differences (Moulas et al., 2013;

* Corresponding author.
E-mail address: centrella.stephen@uni-muenster.de (S. Centrella).

https://doi.org/10.1016/j.lithos.2017.11.002
0024-4937/© 2017 Elsevier B.V. All rights reserved.

Tajčmanová, 2015; Tajčmanová et al., 2014, 2015; Vrijmoed and Podladchikov, 2015), which are directly related to the mechanical properties of the deforming rocks. Variation of mineral assemblages on a small scale has been attributed to such local pressure variations which are a function of the stress direction and material properties (Vrijmoed and Podladchikov, 2015). This concept of a local pressure variation at the grain scale is controversial and earlier studies suggested that the magnitude of pressure deviation from the lithostatic value is small and almost insignificant if rocks are assumed to be weak such that the differential stress that controls natural deformation is small (e.g. <100 MPa) (Brace et al., 1970; Burov et al., 2001; Jolivet et al., 2003). More recently, Schmalholz and Podladchikov (2013) have shown that low viscosity zones may develop significant over- or under-pressure despite their low effective shear stress. A comprehensive review of the arguments for and against a significant effect of non-lithostatic pressure differences on rheology has been recently published (Tajčmanová et al., 2015).

Another model highlighting the importance of stress generation by hydration has been presented by Wheeler (2014). As a function of the pathways of the fluid and the consequent reactions between different minerals, the differential stresses may produce assemblages that would otherwise be interpreted as higher or lower pressure than the actual pressure. This model is also currently being been challenged and debated (Fletcher, 2015; Hobbs and Ord, 2015; Schmalholz and Podladchikov, 2014; Tajčmanová et al., 2015; Wheeler, 2015a, 2015b). Whatever the ultimate explanation, local stress variations in mineral reaction products during hydration have been observed in a number of studies (Jamtveit et al., 2009; Malvoisin et al., 2012; Okamoto et al., 2011; Ostapenko, 1976) but their implications are yet to be fully understood.

In this paper we document a further example where different chemical reactions take place at different microstructural sites within a single crystal undergoing hydration and deformation. Our study is based on a sample from an outcrop in the Bergen Arcs, western Norway, where eclogite and amphibolite-facies hydration events associated with the Caledonian Orogeny (420 Ma) transect older anorthositic granulite-facies rocks (930 Ma). The Bergen Arcs are well known for preserving partially hydrated lower-crustal granulites where the contact between the granulite and the hydrated eclogite and amphibolite can be very sharp (Austrheim, 1987; Boundy et al., 1992; Centrella et al., 2015, 2016). These two hydrated facies are related to the formation of shear zones along which fluid has migrated and reacted with the granulite (Austrheim, 1987). Pseudotachylites are common throughout the region and may be related to the first stages of reaction and fracturing that facilitated fluid infiltration (Austrheim, 2013; Austrheim and Boundy, 1994; Lund and Austrheim, 2003). The Bergen Arcs represent an exceptional window into the lower crust, and the abundant preservation of arrested reaction textures makes it an exceptional place to study the interplay among fluid infiltration, deformation, and reaction-driven stress generation.

In this paper we describe an example of a hydration interface on a hand-specimen scale between a relatively dry anorthositic granulite and an amphibolite-eclogite facies overprint. Within the granulite an Al-rich clinopyroxene with a garnet corona has been fractured by a fault and partially hydrated. Within the Al-rich clinopyroxene crystal, a

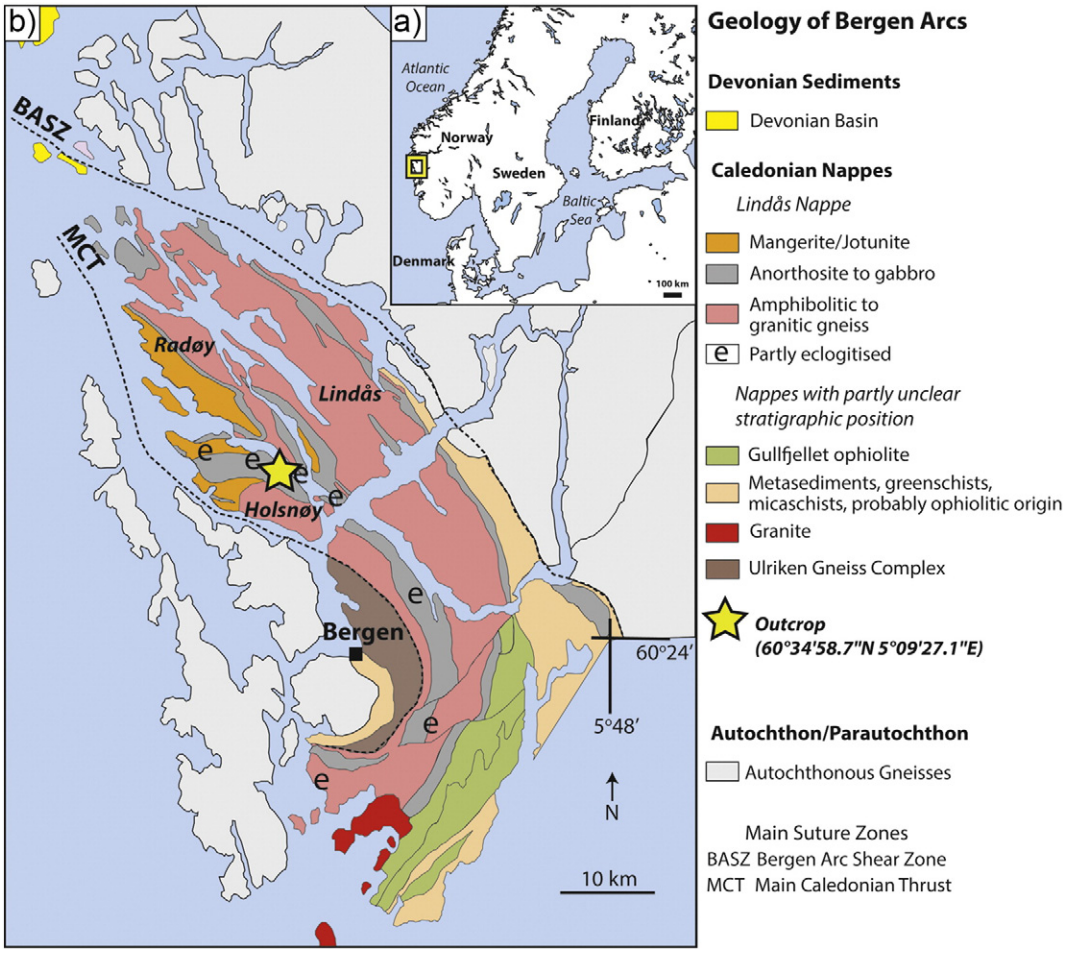

Fig. 1. a) Location of the Bergen Arcs in Norway. b) Geological map of the Bergen Arcs with location of the outcrop of this study (yellow star).

network of deformation bands is associated with a new generation of garnet and a low-Al clinopyroxene while other parts of the same crystal are replaced by chlorite along cleavage planes. We investigate the spatial and possible temporal relationships between these two parageneses. Textural and chemical analyses have been carried out by scanning electron microscopy (SEM), electron microprobe analysis (EMPA) and electron backscatter diffraction (EBSD) within a single grain of clinopyroxene.

2. Geological setting

In the Bergen Arcs, W-Norway, anhydrous Precambrian granulites are intermingled with Caledonian eclogite and amphibolite-facies assemblages. The Caledonian metamorphism at ~430 Ma is associated with shear zones and veins and about 90% of the granulite is hydrated (Andersen et al., 1991). The lack of re-equilibration in the remaining granulite has been attributed to its anhydrous nature (Austrheim, 1987) or that the thermal pulses were too short-lived to allow re-equilibration (Camacho et al., 2005). The amphibolites are generally interpreted as having formed during uplift and the main difference in major element chemical composition between the eclogites and amphibolites is a higher volatile content (loss on ignition – LOI) in the latter. From U/Pb dating on zircon in eclogite and amphibolite, the ages of metamorphism cannot be easily distinguished (~428 Ma) whereas using Rb/Sr, Sm/Nd, Ar-Ar on phengite, multi-mineral isochron ages, the amphibolite facies metamorphism seems to be younger (~414 Ma) (Glodny et al., 2008; Schneider et al., 2008). Boundy et al. (1992) show that the amphibolite-facies metamorphism occurs along brittle fractures where a fluid enters and reacts through the granulite. Andersen et al. (1991) estimated the amphibolite-facies conditions at 4–7 kbar and 575–675 °C and Boundy et al. (1996) at 10–12 kbar and 650–690 °C. The original granulite was formed ~930 Ma (Bingen et al., 2001; Cohen et al., 1988; Schneider et al., 2008) at a pressure around 10 kbar and a temperature around 800–850 °C (Austrheim, 1987; Austrheim and Griffin, 1985).

2.1. Sample description

The outcrop is located in the island of Hølsnoy (68°34′58.7″N 5°0.9′ 27.1″E, Fig. 1). The granulite facies anorthosites of the Bergen Arcs contain, in addition to plagioclase, Al-rich clinopyroxenes, garnet, locally S-rich scapolite, orthopyroxene (located in the core of some lenses with the garnet coronas) and spinel (pleonaste). The hand specimen studied here has a granulitic foliation visible by the elongated shape of the clinopyroxene aggregates (Fig. 1). Some of the pyroxene lenses are rimmed by garnet, presumed have formed as part of the corona structures formed in the granulites through much of the Bergen Arcs. The garnet coronas have been extensively described and are formed by reaction between olivine and plagioclase during the granulite facies metamorphism (Austrheim and Griffin, 1985; Griffin and Heier, 1973).

The interface between the dark granulite and the light-coloured hydrated granulite is sharply defined by the colour change in the feldspar from lilac-brown to milky-white (Fig. 2a and b). Mukai et al. (2014) have described the milky, turbid feldspar in a similar sample from this area as a breakdown of the intermediate composition plagioclase to a complex intergrowth of Na-rich and Ca-rich plagioclase domains and the presence of many inclusions. The turbidity in feldspars has long been associated with the presence of micropores and inclusions associated with replacement reactions (Parsons and Lee, 2009; Walker et al., 1995). The hydration front is not deformed and the overall fabric of the rock is unchanged. Lenses of clinopyroxenes in the hydrated part are crosscut by small microfaults that do not form in the granulite (Fig. 2c and d). Associated to these microfaults, a network of garnet appears within each individual crystal that composes the Cpx lens

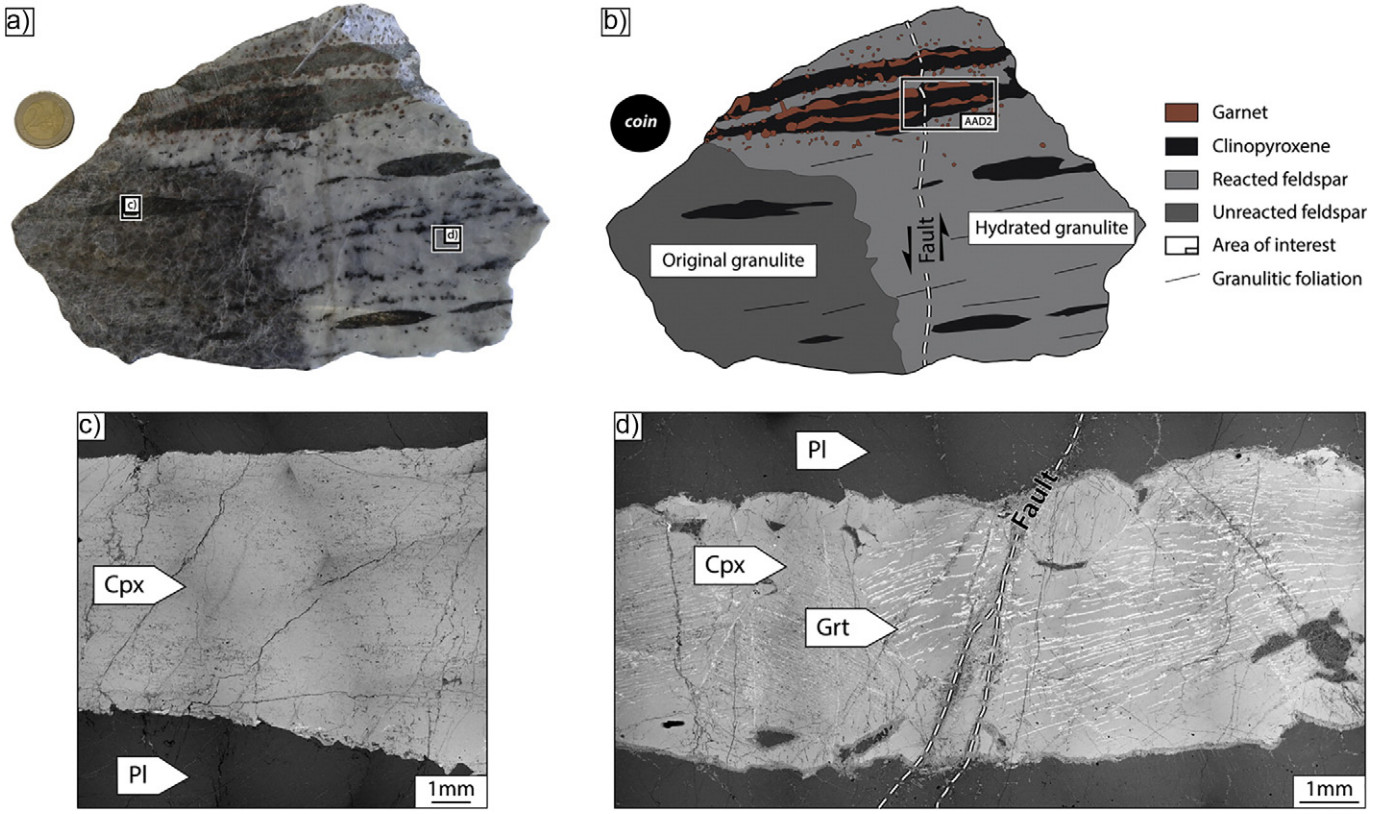

Fig. 2. Photograph of the hand sample of (a) the granulite and (b) the interpretative sketch. SEM backscatter image of a Cpx lens in the original granulite (c) and the hydrated part (d).

(Fig. 2d). All of these features are related to the hydration event with the formation of lower-grade and hydrous phases such as epidote, chlorite, mica and amphibole throughout the hydrated part of the sample. One major fault cuts the entire hand specimen but is only located in the hydrated part, passing through a pyroxene lens and displacing it by several millimetres (Fig. 2b). The area around this fracture (AAD2 in Fig. 2b) is the focus of this paper.

3. Methods

Thin sections were studied by optical microscopy, scanning electron microscopy (SEM: JEOL JSM 6610LV), and by electron probe microanalysis (EPMA: JEOL 8530F) for quantitative element mapping at the University of Münster. The standard microprobe conditions were 15 nA and 20 keV for quantitative analysis and 50 nA and 15 keV for

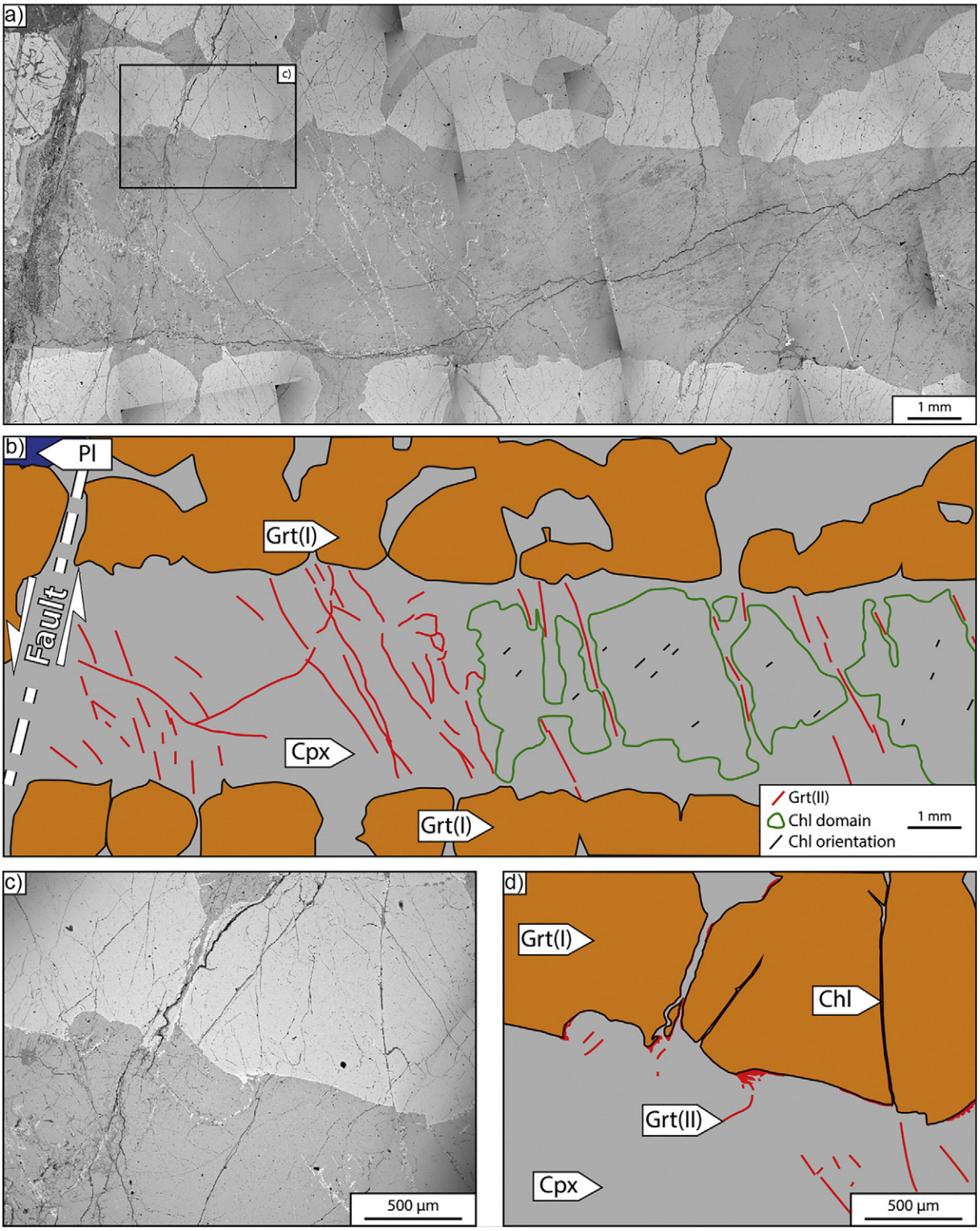

Fig. 3. a) SEM backscatter image of a part of the Cpx lens with the interpretative sketch (b). c) SEM backscatter image of the Grt(I) recrystallizing into Grt(II) with the interpretative sketch (d).

the element mapping. Standards used for quantitative measurement were jadeite (Na), kyanite (Al), sanidine (K), forsterite (Mg), hypersthene (Si), diopside (Ca), rhodocrosite (Mn), rutile (Ti), fayalite (Fe), and chromite (Cr). The software XMapTools 2.2.1 (Lanari et al., 2014) was used to quantify electron microprobe X-ray maps and to calculate the composition of specified areas within maps to follow the evolution of the local composition. Electron backscatter diffraction (EBSD) analysis with EDS data were carried out at the John de Laeter Centre, Curtin University using a field emission TESCAN MIRA3 SEM. EBSD data were acquired using an Oxford Instruments AZtec EBSD and EDS system. Post-processing of EBSD data to produce various property maps and pole figures was done using Oxford Instruments Channel 5.11 software. Pole figures are reported as lower hemisphere, equal-area projections. In all EBSD maps, a 6 nearest-neighbour noise zero solution noise reduction has been applied. To determine the pressure-temperature conditions of mineral assemblages, we used the software Theriak-Domino (de Capitani and Petrakakis, 2010) with the thermodynamic database tc55 (Holland and Powell, 1998) and subsequent updates (Baldwin et al., 2005; Coggon and Holland, 2002; Diener et al., 2007; Holland and Powell, 2003; Kelsey et al., 2005; Mahar et al., 1997; White et al., 2000, 2002, 2007). We use all the solid solutions that take Fe^{3+} into account.

4. Results

4.1. Optical microscopy and scanning electron microscopy (SEM) petrography

A merged image of backscattered electron images of the lens of clinopyroxene associated with a garnet corona is shown in Fig. 3a and b (AAD2, location in Fig. 2b). The clinopyroxene lens is polycrystalline and made up of grains approximately 6 mm in size. The fault drawn in Fig. 2 is located on the left of Fig. 3a and b and shows a displacement indicated by the white arrows. The clinopyroxene (Cpx) located between the two layers of garnet (Grt(I)) contains a network of new garnet grains along kinks (Grt(II), red lines in Fig. 3b) and chlorite (Chl) along Cpx cleavages (mostly inside the green areas in Fig. 3b). Mineral abbreviations are after Kretz (1983).

The new generation of Grt(II) forms within the kink-bands that form a sub-parallel network through the Cpx lens while Chl forms along cleavage planes of the Cpx at a steep angle to the garnet-bearing fractures. In a few places, Grt(I) seems to recrystallize into Grt(II) at the interface with Cpx. Some kink-bands continue through Grt(I) via fractures filled with Chl (Fig. 3c and d). The domains where Chl is present (in green) are generally located in the core of the Cpx, away from the rim adjacent to the Grt corona (Figs. 3, 4a). The optical extinction of the Cpx is undulose in every individual grain present in the lens. The Cpx crystal in contact with the main fault shows strong undulose extinction in the entire crystal and does not contain any Chl. All along the Cpx lens, Chl is absent where the undulose extinction is strong. At the tip of the kink-bands containing the new generation of Grt(II), there is well-developed undulose extinction in the Cpx (between the two dashed lines in Fig. 4b). This dark area starts at the tip and continues along the kink band through the Cpx crystal. Neither Chl nor Grt(II) are present in this domain. The zone of well-developed undulose extinction is as wide as the kink itself (100–150 μm).

Within the domains that contain chlorite, local variation of the optical extinction in the Al-rich Cpx is indicated by white linear features, approximately 50 μm wide (Fig. 5a, b), that are sub-parallel to each other and also to the kink-banding network. The angular difference in the extinction position relative to the Cpx matrix is around 5°. Along these linear domains Chl is conspicuously absent nor do the domains generally contain Grt(II). In parts of the crystal where Grt(II) forms within the

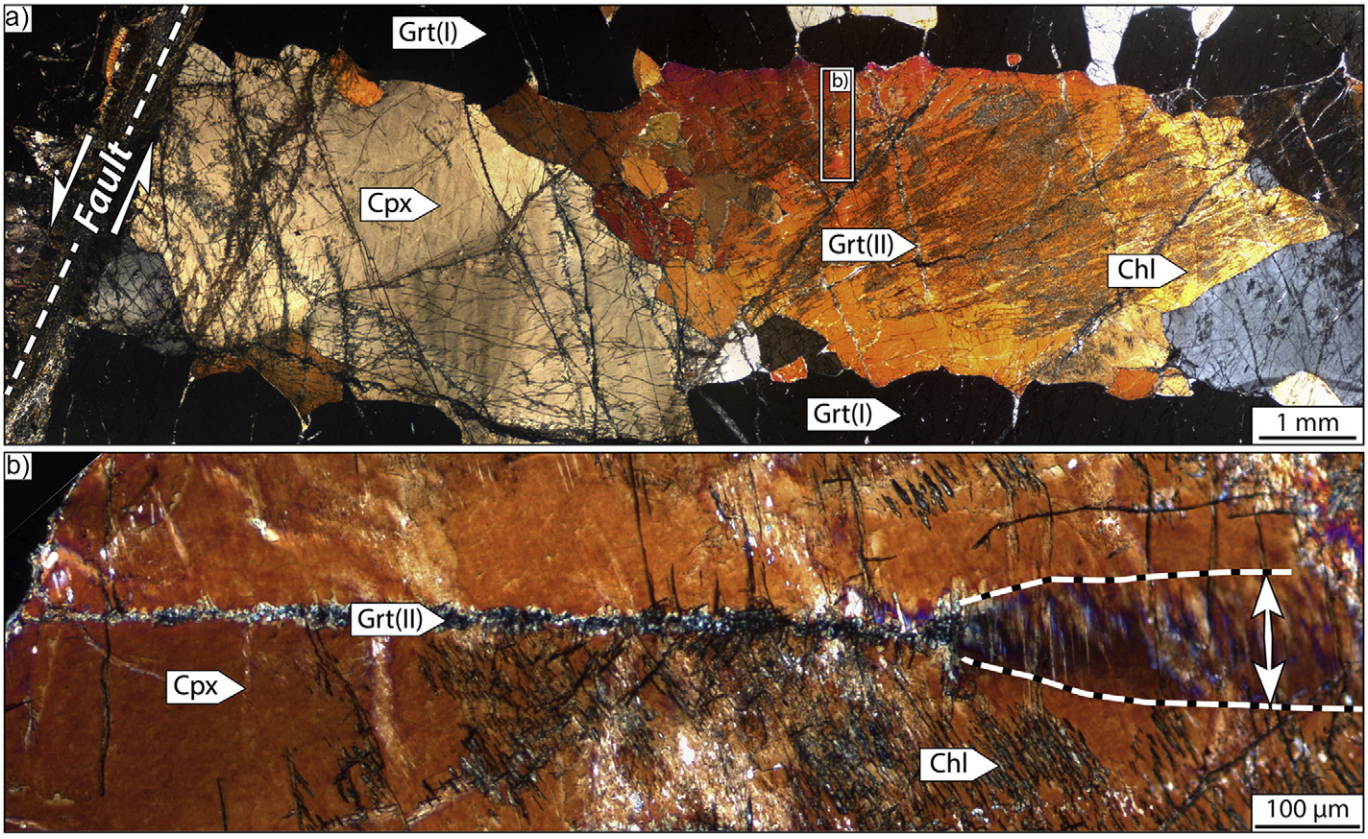

Fig. 4. a) Crossed polarized microscope image of the clinopyroxene lens surrounded by garnet with location of the main fault. b) Crossed polarized microscope image of the new generation of garnet (Grt II) along a fracture where the clinopyroxene at the tip shows strong undulose extinction (white arrow between dashed lines). Image b) is rotated 90° anticlockwise relative to the orientation in a).

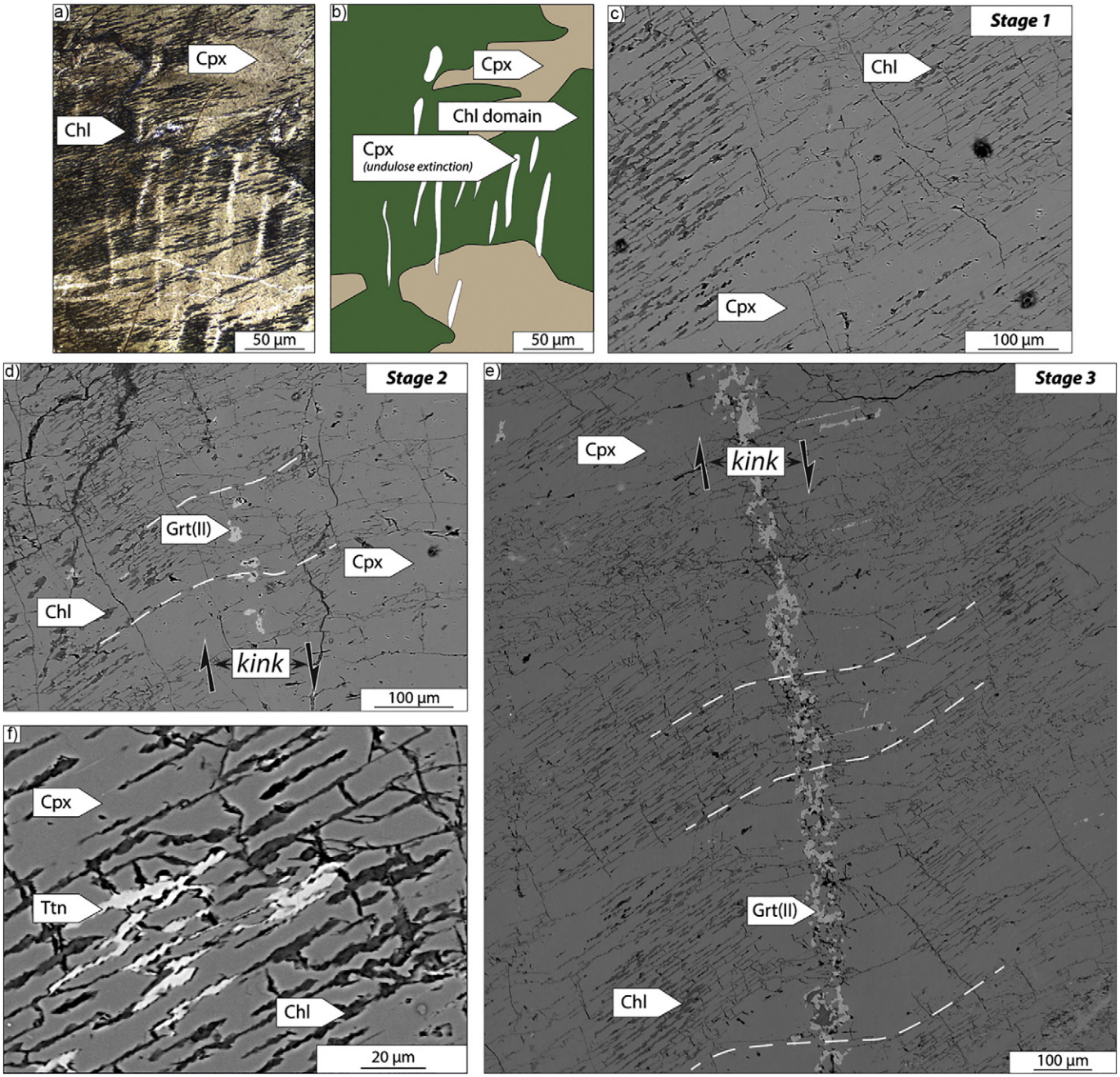

Fig. 5. a) Crossed polarized microscope image of the undulose extinction in the Al-rich Cpx within the Chl domain and (b) its schematic sketch. c) Backscattered image localized in these undulose extinction regions. d) SEM Backscattered image localized in another undulose extinction domain where garnet and kink deformation start to form. e) SEM backscatter image with representation of a kink deformation and the associated deformation (dashed lines). f) SEM backscatter image showing where titanite (Ttn) is located within the Chl domain.

Chl-free linear domains, deformation is visible as a kink band shown by the curved displacement of the Cpx cleavages (Fig. 4d, e). The Grt(II) grains are irregular in shape and are distributed along these kink-bands. The main difference between Fig. 5d and e is the amount of Grt(II) within the kink. Fig. 5e represents the typical kink banding visible in Figs. 3 and 4. Within the Chl domain, some calcite and titanite are present and are always associated with Chl formation along the cleavage planes of the Cpx (Fig. 5f).

4.2. Electron probe microanalysis

Grt(I) located in the corona around the Cpx does not have any inclusions and has a constant composition of $Alm_{33}Prp_{44}Grs_{25}Adr_3$ (Table 1 analyses 72 and 73), similar to garnets described from this locality by Erambert and Austrheim (1993). The Cpx composition is also constant throughout most of the grains, including near the Chl lamellae as well as near the Grt corona (Table 1 analyses 558 and 561).

An unusual feature of this Cpx is the high Al content (11 wt% Al_2O_3), referred to here as Al-rich Cpx. However, along the linear features shown in Fig. 5 and close to the Grt(II), the clinopyroxene has a different composition. The equivalent quantitative Al_2O_3 maps from the same area show this more clearly (Fig. 6). In every case the clinopyroxene along the linear domains and associated with Grt(II) has a lower Al and Na but higher Mg, Ca and Si composition. The Al composition of the Cpx decreases from 11 wt% to 8 wt% Al_2O_3 in this central part (Fig. 6b). The small black spots within the linear feature (Fig. 6a)

Table 1
Microprobe analyses of garnet, clinopyroxene and chlorite. Each structural formula has been calculated using the software AX of Holland and Powell (2006). Estimation of the ferric iron (Fe^{3+}) was made following the calculation described in Holland and Powell (1990, 1998).

	Garnet					Clinopyroxene					Chlorite				Amphibole	
Location	Grt(I)	Grt(I)	Grt(II)	Grt(II)	Grt(II)	Near Chl	Near Grt(I)	Kink	Kink	Kink	In Cpx(I)	In Cpx(I)	Kink	Kink	Kink	Kink
Analyses	72	73	82	85	90	558	561	566	576	577	543	551	1	2	3	4
SiO_2	40.03	40.19	38.34	39.20	38.96	48.96	49.72	53.11	54.23	53.15	29.89	30.18	31.15	31.70	43.50	43.36
TiO_2	0.06	0.06	0.06	0.02	0.07	0.36	0.33	0.08	0.13	0.16	0.00	0.04	0.01	0.01	0.50	0.56
Al_2O_3	22.37	22.19	21.65	21.73	21.71	11.20	11.08	3.51	2.58	4.62	18.27	17.90	16.21	16.02	15.28	15.07
Cr_2O_3	0.00	0.00	0.00	0.00	0.00	0.00	0.01	0.01	0.00	0.00	0.00	0.02	0.02	0.02	0.00	0.00
FeO	16.31	15.57	21.98	20.48	20.39	6.06	6.09	5.54	5.23	5.83	15.38	14.38	15.84	16.92	11.89	12.36
MnO	0.38	0.33	0.33	0.31	0.31	0.07	0.06	0.05	0.04	0.02	0.07	0.06	0.05	0.06	0.15	0.15
MgO	11.70	12.21	7.61	8.24	8.36	10.44	10.76	14.02	14.43	13.31	22.65	23.67	22.26	21.82	12.44	12.53
CaO	8.10	8.15	10.21	10.07	10.28	20.24	19.82	21.81	22.54	21.42	0.28	0.39	0.51	0.41	10.45	11.00
Na_2O	0.00	0.00	0.00	0.00	0.00	2.27	2.70	1.86	1.36	1.55	0.01	0.01	0.06	0.07	3.37	3.38
K_2O	0.00	0.00	0.00	0.00	0.00	0.02	0.03	0.00	0.00	0.02	0.01	0.00	0.02	0.02	0.00	0.00
Totals	98.95	98.70	100.18	100.05	100.08	99.62	100.60	99.99	100.54	100.08	86.56	86.65	86.13	87.05	97.58	98.41

	Normalized to 12 oxygens						Normalized to 6 oxygens						N. to 14 oxygens				N. to 23 oxygens	
Si	2.990	2.979	2.927	2.978	2.957	Si	1.782	1.796	1.934	1.971	1.943	Si	3.009	3.020	3.158	3.193	6.293	6.255
Ti	0.004	0.003	0.004	0.001	0.004	Ti	0.010	0.009	0.002	0.004	0.004	Ti	0.000	0.003	0.001	0.001	0.054	0.061
Al	1.970	1.939	1.949	1.946	1.943	Al^{IV}	0.208	0.195	0.064	0.025	0.053	Al	2.168	2.112	1.938	1.902	2.606	2.564
Cr	0.000	0.000	0.000	0.000	0.000	Al^{VI}	0.273	0.277	0.087	0.086	0.146	Cr	0.000	0.002	0.001	0.002	0.000	0.000
Fe^{3+}	0.042	0.095	0.189	0.094	0.135	Cr	0.000	0.000	0.000	0.000	0.000	Fe^{3+}	0.000	0.000	0.000	0.000	0.326	0.291
Fe^{2+}	1.019	0.965	1.208	1.207	1.160	Fe^{3+}	0.097	0.108	0.109	0.037	0.018	Fe^{2+}	1.295	1.204	1.343	1.425	1.113	1.201
Mn	0.024	0.021	0.022	0.020	0.020	Fe^{2+}	0.112	0.076	0.060	0.122	0.160	Mn	0.006	0.005	0.004	0.005	0.018	0.018
Mg	1.303	1.349	0.866	0.933	0.946	Mn	0.002	0.002	0.002	0.001	0.001	Mg	3.398	3.530	3.364	3.275	2.683	2.693
Ca	0.648	0.647	0.835	0.820	0.836	Mg	0.566	0.579	0.761	0.782	0.725	Ca	0.030	0.042	0.056	0.044	1.621	1.700
Na	0.000	0.000	0.000	0.000	0.000	Ca	0.789	0.767	0.851	0.878	0.839	Na	0.001	0.003	0.011	0.013	0.945	0.947
K	0.000	0.000	0.000	0.000	0.000	Na	0.160	0.189	0.131	0.096	0.110	K	0.001	0.000	0.003	0.003	0.000	0.000
						K	0.001	0.001	0.000	0.000	0.001							
Sum	8	8	8	8	8		4	4	4	4	4		9.91	9.92	9.88	9.86	15.66	15.73
XPrp	0.44	0.45	0.30	0.31	0.32	XHed	0.11	0.08	0.06	0.12	0.16	X_{Mg}	0.72	0.75	0.71	0.70	Type Prg	Prg
XAlm	0.34	0.32	0.41	0.41	0.39	XJd	0.06	0.08	0.02	0.06	0.09							
XSps	0.01	0.01	0.01	0.01	0.01	XDi	0.52	0.54	0.74	0.75	0.68							
XGrs	0.20	0.17	0.19	0.23	0.22	XCaTs	0.21	0.20	0.06	0.02	0.05							
XAdr	0.02	0.05	0.09	0.05	0.07	XAcm	0.10	0.11	0.11	0.04	0.02							
X_{Mg}	0.56	0.58	0.42	0.44	0.45	X_{Mg}	0.83	0.88	0.93	0.87	0.82							

where the aluminium concentration decreases may be porosity but could also be a consequence of loss of small Grt(II) grains during polishing. The Cpx composition is only altered along the thin band next to the Grt(II). In most cases the composition changes in a stepwise fashion between the Al-rich Cpx and low-Al Cpx indicating that diffusion following recrystallization was not significant. This is supported by profiles (Supplementary material 1). In some places, this boundary is more diffuse and shows a gradational change in Al_2O_3 although this could also be due to an inclined interface between the two Cpx populations. When the kink and Grt(II) formation are further developed (Fig. 5d), the Cpx associated with the Grt(II) has an even lower Al_2O_3 content of ~5 wt% (Fig. 6d). The Grt(II) located in the kink has an average composition of $Alm_{41}Prp_{32}Grs_{21}Adr_7$ with no visible chemical zoning (Table 1 analyses 82). These Grt(II) grains are never in contact with the Al-rich Cpx matrix and the low-Al Cpx makes a mantle perfectly surrounding the garnet crystals.

Fig. 6e, f, g show a phase map, a compositional map of Al_2O_3 (in wt%) and a map of the diopside end-member fraction of the Cpx surrounding the Grt(II) of the same area as in Fig. 5e. In comparison to the kink in the previous figure (Fig. 6d), the surrounding Cpx has lost even more Al and Na but gained more Mg, Ca and Si (Table 1 analyses 566, 576 and 577). The Grt(II) located in the kink has the same composition as that described in Fig. 6d ($Alm_{41}Prp_{32}Grs_{21}Adr_7$) with no visible chemical zoning (Table 1 analyses 85 and 90) and is always mantled by the low-Al Cpx. In Fig. 6e, f, g there are also small linear features containing Grt(II) and low-Al Cpx at approximately right angles to the main kink but within the Chl-free zone that extends for ~200 μm parallel to the kink. The composition of the Chl is also listed in Table 1. No Chl is present in this central part of the kink except in one unique area located in the lower part of the figure (in blue in the middle of the kink in Fig. 6e). This Chl has a different chemical composition to that in the Chl domain (see Table 1 analysis 2) and has possibly formed during later alteration.

Based on the nomenclature of Morimoto (1988) and the Al content of the structural formulae (Al > 0.1), the Al-rich and the low-Al Cpx are both aluminian diopside. The diopside component is 25% higher in the low-Al Cpx (0.75) than in the Al-rich Cpx (0.5) (Table 1 and Fig. 6g). The quantitative aluminium map and diopside end-member map were obtained using the structural formulae functions provided with the software XMapTools.

At the tip of the kink shown in Fig. 4b, the amphibole pargasite (Prg) is also present. This is confirmed by quantitative analysis (Table 1) and imaged in Fig. 7. Pargasite is surrounded by Grt(II) and low-Al Cpx and but is not in contact with the high Al-rich Cpx. The Chl-free region beyond the tip of the kink where the extinction is undulose also contains small grains of pargasite (shown in the lower part of Fig. 7b as lines with a slightly higher Al content). Pargasite is a calcic-amphibole that contains (Na + K) > 0.5 in the A-sites and between 6.5 and 7.5 Si atoms per formula unit (Table 1) (Leake, 1978). Moreover, the Al site content > 1 indicates that it is an alumina-pargasite. Based on a more recent nomenclature, Hawthorne et al. (2012) define pargasite with (Na + K + 2Ca) > 0.5 in the A-sites and (Al + Fe^{3+} +2Ti) between 0.5 and 1.5 in the C-sites. However the occurrence of pargasite is uncommon in this sample and has only been observed in this one case at the termination of a kink.

4.3. Electron backscatter diffraction (EBSD)

Crystallographic orientation/information of minerals has been collected with EBSD along the region shown in Fig. 5e. The EDS map for Al overlain with the band contrast map (nonvisible) shows that the low-Al Cpx located in the centre of the kink has a high density of grain

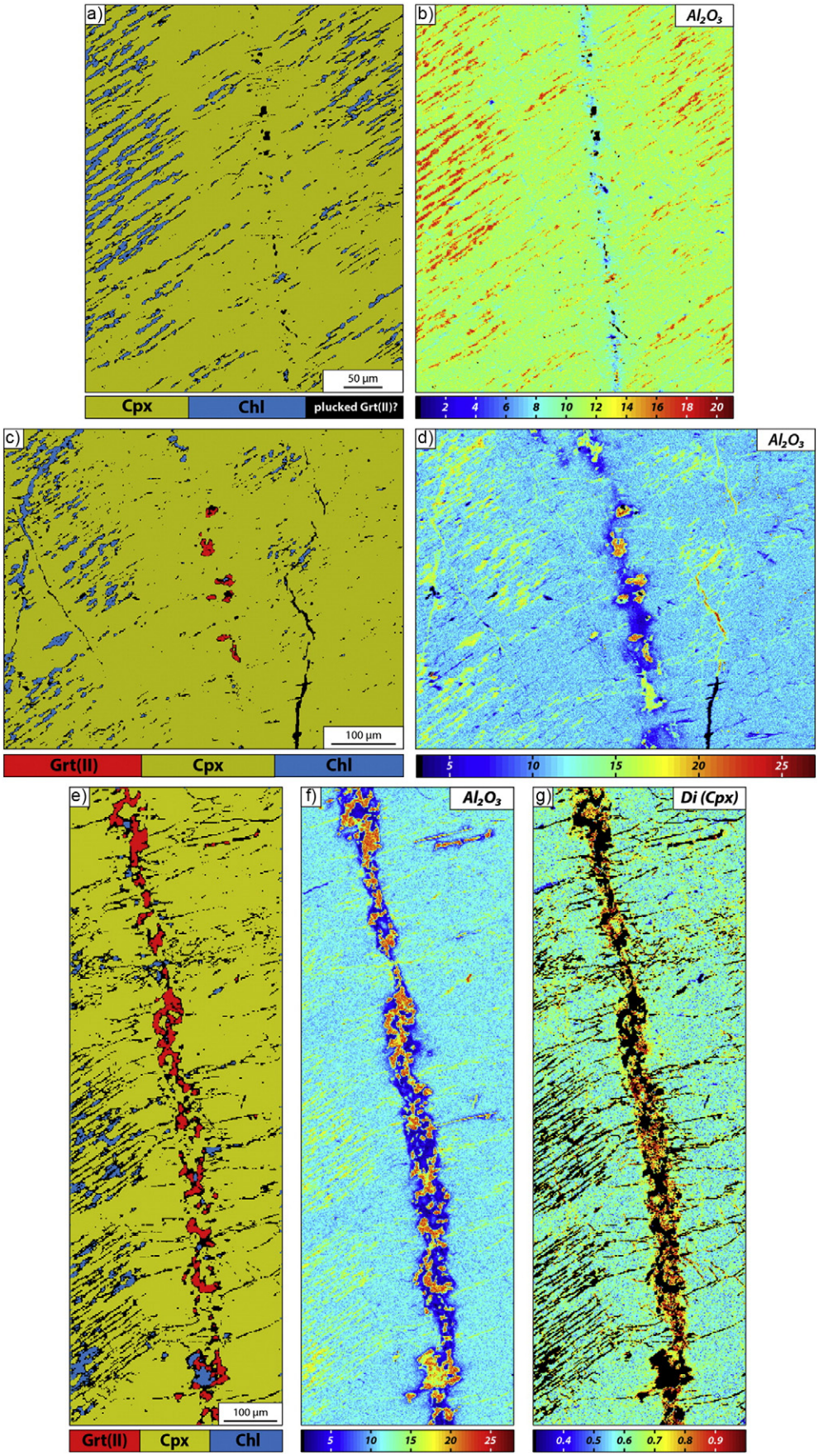

Fig. 6. a) Phase map presented in Fig. 4c, d, c and its associated quantitative microprobe map of Al_2O_3. c) Phase map presented in Fig. 4d and its associated quantitative microprobe map of Al_2O_3 (wt%). e) Phase map located in the kink presented in Fig. 4f. f) Quantitative microprobe map of Al_2O_3 and g) composition of the Cpx expressed as the diopside end-member concentration through the map. The maps were obtained using the software XMapTools v. 2.1.1 from Lanari et al. (2014).

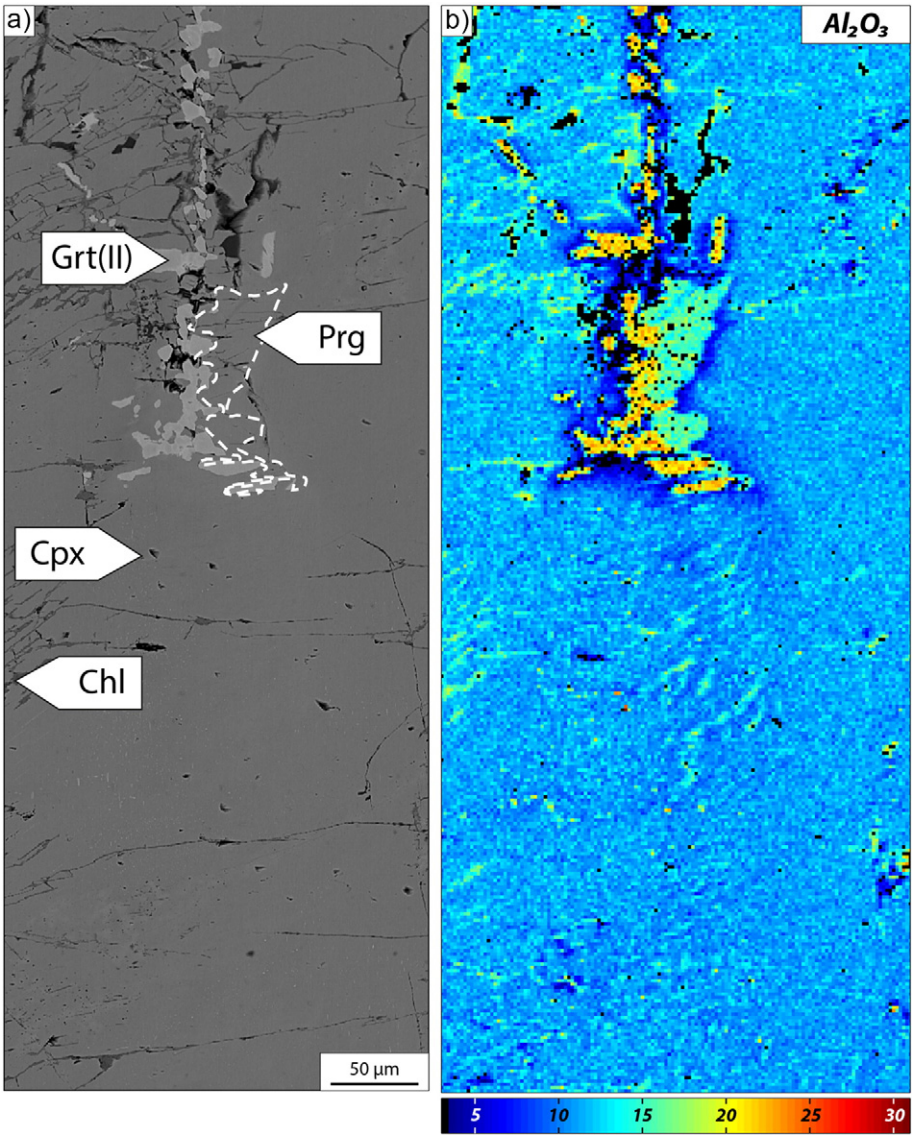

Fig. 7. a) Backscatter SEM image of picture presented in Fig. 3b and (b) its associated quantitative microprobe map in Al_2O_3. Pargasite is represented in the dashed line domain.

boundaries (Fig. 8a) and individual Cpx grains are smaller than 50 µm. Low and high angle grain boundaries are shown as red and white lines in the low-Al Cpx region in Fig. 8a. The band contrast map transparently overlain with the texture map (Fig. 8b) shows that the low-Al Cpx has a misorientation of up to 25° compared to a reference point in the Al-rich Cpx (white cross in Fig. 8b). Optical microscopy shows that the area in the kink surrounding the Grt(II) + low-Al Cpx exhibits undulose extinction. With a reference point in this domain, Fig. 8c shows that the Al-rich Cpx around Grt(II) + low-Al Cpx is misoriented by about 1° relative to the bulk of the pyroxene that contains the Chl. The misorientation of each grain increases from the rim to the core of the structure (Fig. 9a). The pole figure of low-Al Cpx grain orientations (Fig. 9b) suggests that the crystallographic preferred orientation (CPO) is inherited from the parent Al-rich Cpx, based on the progressive misorientation of all axes from primary Al-rich Cpx. The Grt(II) grains along the kink show weak CPO (Fig. 9c). The width of these deformation bands is related to the amount of Grt(II) + low-Al Cpx formed, increasing from ~100 µm (Figs. 5c, 6a) to ~200 µm (Figs. 5e, 6e).

The EBSD data located from around the tip of the kink is shown in Fig. 10. The grain size and misorientation of this low-Al Cpx grains is similar to the low-Al Cpx previously presented in Fig. 8. The region beyond the tip that shows strong undulose extinction in Fig. 4b, has a misorientation up to 10° relative to the reference point (white cross in Fig. 10b), increasing from the rim to the centre but relatively constant along its length (Fig. 10c). Pargasite at the end of the kink is composed of grains around 25 µm long and <10 µm in width. Fine trails of the pargasite, best seen in Fig. 10a as grey lines, also form within the misoriented Cpx region. The low-Al Cpx inherits the crystallographic information of the parent Al-rich Cpx (Fig. 10d) and the Grt(II) grains show only weak CPO (Fig. 10e).

4.4. Modelling of phase equilibria

We use standard thermodynamic modelling to estimate the thermodynamic pressure and the temperature of formation for the specific assemblage Grt(II) + low-Al Cpx. The equilibrium models are computed using the local bulk composition of the domain Grt(II) + low-Al Cpx (Table 2). To estimate the excess of oxygen in the assemblage, we constructed a P-X diagram for 630 °C (Fig. 11a). This temperature corresponds to the average temperature estimation for the amphibolite facies conditions for the Bergen Arcs (Andersen et al., 1991; Boundy et al., 1996). To better constrain the excess of oxygen, we used Grt isopleths ($Alm_{41}Prp_{32}Grs_{21}$) and found an excess of ~0.36 mol%.

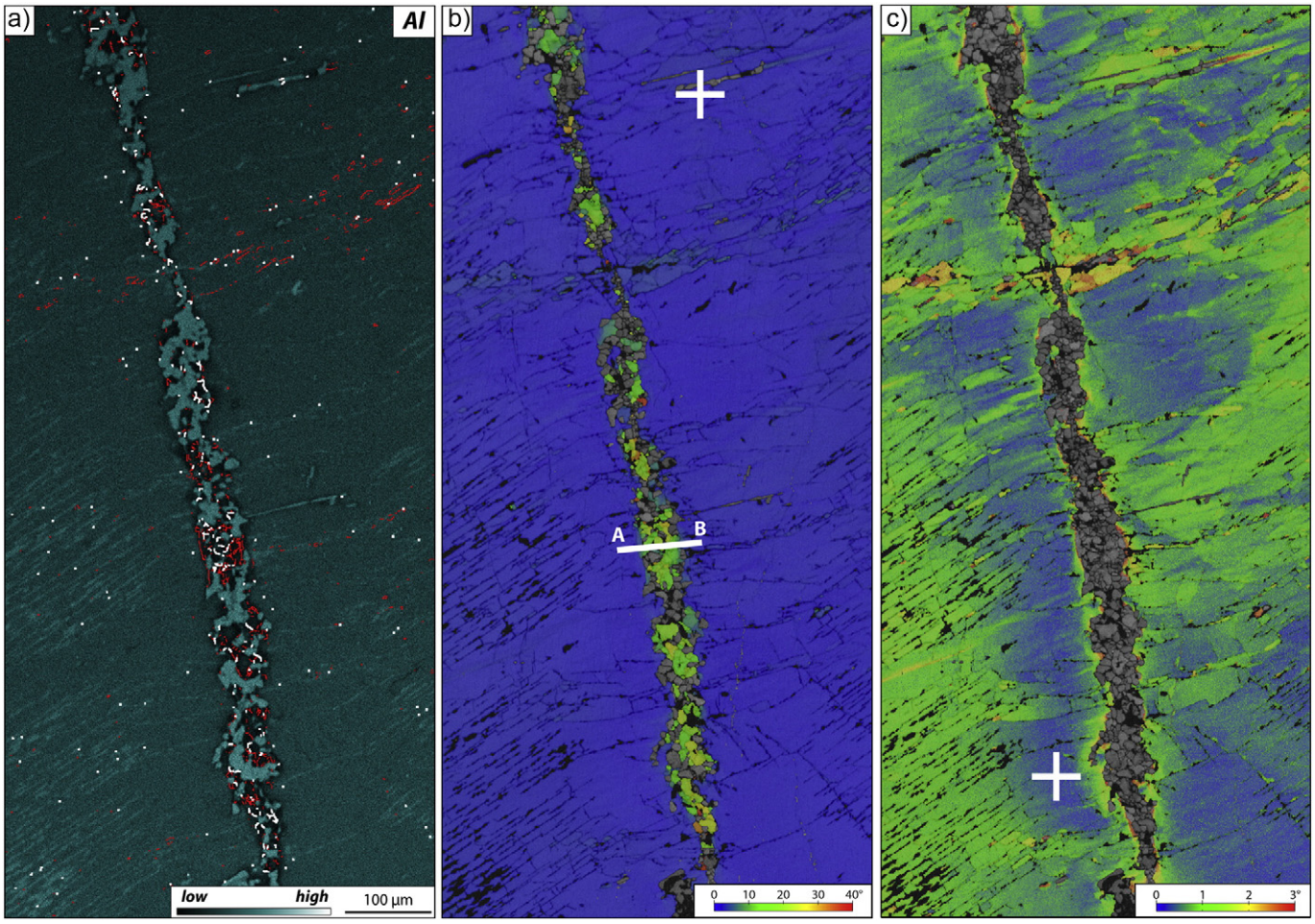

Fig. 8. EBSD data from Cpx. a) EDS map of Al. Red lines represent the grain boundary between 2 and 10° and white lines > 10°. b) Texture map overlain with band contrast for Cpx. Step size of the maps was 1 μm. c) Texture map overlain with band contrast for Cpx. Step size of the maps was 1 μm. Reference crystal is represented by the white cross.

The corresponding anhydrous isochemical equilibrium phase diagram for the assemblage Grt(II) + low-Al Cpx as a function of P and T is presented in Fig. 11b. The relevant field is shown in light grey by the assemblage Grt-Cpx-Qtz (in bold). Although quartz (Qtz) is predicted to be stable in this field and has not been found in the sample, it represents <3 vol% of the calculated assemblage. Qtz is systematically predicted to be stable with Grt and Cpx. Sensitivity tests were performed at 650 °C and 25 kbar using the method of Lanari and Engi (2017) that automatically change the shape of the selected domain to estimate an uncertainty on the local bulk composition. The average modal abundance of Qtz predicted at 650 °C and 25 kbar is 2.64 ± 0.24 vol%. This test demonstrates that the presence of Qtz cannot be explained by the uncertainty in the bulk rock composition. For a further check, we calculated P-X_{SIO2} diagrams for different temperatures (570, 630 and 700 °C), with and without Fe^{3+} in order to see if Qtz would be predicted to be stable. However, if quartz disappears, another phase replaces it such as olivine or magnetite with a higher proportion of Fe^{3+}. In both cases, the composition of garnet and clinopyroxene cannot be reproduced. Therefore the presence of quartz is more likely to be a consequence of uncertainties in the thermodynamic properties or activities in the data.

Using the Grt(II) isopleths to constrain the P-T conditions ($Alm_{41}Prp_{32}Grs_{21}$) and the X_{Mg} of Cpx (~0.91), it appears that this assemblage is stable between 17 and 28 kbar and between 620 and 730 °C (dotted field). The stability field is very dependent on the garnet composition and therefore an average composition of the entire Grt(II) located in the kink was used in the calculation. The largest deviation from the average composition is represented by analysis 90 (Table 1) but is very close to the average.

5. Discussion

The hand specimen presented in Fig. 2 is typical of the type of interface between the granulite protolith and the amphibolite overprint that can be found in many outcrops in the Bergen Arcs. The lenses of the Al-rich Cpx and Grt were formed under granulite-facies conditions of around 10 kbar and 850 °C (Austrheim and Griffin, 1985) at ~930 Ma (Bingen et al., 2001) and were partially hydrated and deformed during the Caledonian continental collision at ~430 Ma (Glodny et al., 2008). The hydration to amphibolite facies metamorphism is often spatially associated with shear zones and/or fracturing. Amphibolite-facies metamorphism occurs along brittle fractures where the fluid infiltrates and reacts into the shear zone through the granulite (Boundy et al., 1992). As in our hand specimen, fractures facilitate fluid infiltration into the rock and this is most clearly seen as the colour change (from lilac-brown to white) in the feldspar as described by Mukai et al. (2014). The fracturing, kink banding and hydration reactions are all broadly associated with the amphibolitisation "event" (Fig. 2c and d) and the sharp interface between the dry granulite and the hydrated amphibolite suggests a discrete event that was terminated in both time and space at this interface. Within the Al-rich Cpx surrounded by a Grt corona, a network of kink banding is formed.

The deformation features within the Al-rich Cpx could be interpreted as the result of the adjacent fault (Fig. 3) as a consequence of the Cpx

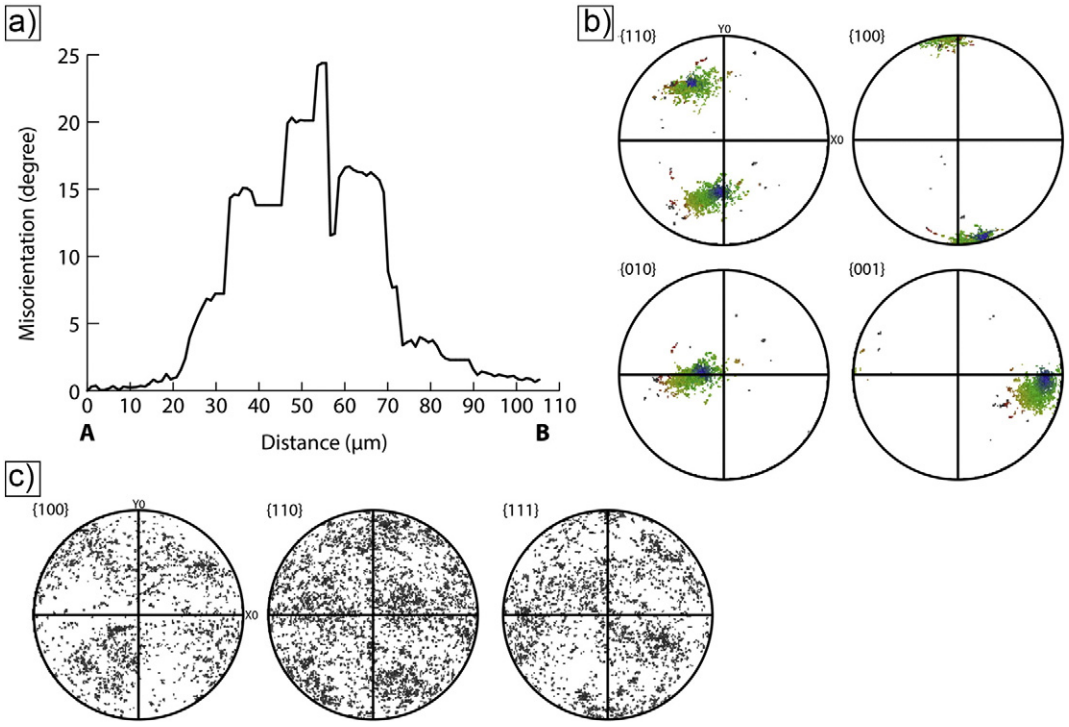

Fig. 9. Misorientation profile of the white line drawn in (b). Reference crystal is represented by the white cross in (b). d) Lower hemisphere equal area projection showing the Cpx crystal orientations (524,335 data points). Colours in the map b) and the pole figures d) are correlated. e) Lower hemisphere equal area projection showing crystal orientations (16,495 data points) of the Grt(II) grains along the fracture.

being sandwiched between two competent layers of garnet (Grt(I)). The consistent orientation of the kinks across the Al-rich Cpx crystals of varying orientation shows that the deformation is not crystallographically controlled in this case. The observed microstructures and the local changes in mineralogy could be interpreted as an evolution determined either as a time sequence or as a result of contemporaneous stress variations within the crystal. Fig. 5 supports both ideas, from:

(i) the misorientation along linear features within the Al-rich Cpx, where no Chl exists but a central spine along the linear domain is replaced by a Cpx lower in Al (Fig. 6f), to
(ii) the progressive formation of a recognisable kink where Grt(II) + low-Al Cpx are formed (Fig. 5d), and
(iii) the final stage where the Al-content of the Cpx is reduced even further as the amount of Grt(II) formed along the kink increases (Fig. 5e).

A notable observation is that the linear features in Fig. 5a, b are parallel to the kink bands containing the Grt(II) suggesting a common origin of the stress. The local deformation along the kink bands is shown by the misorientation in the Al-rich Cpx in a 200 μm wide domain on either side of the Grt(II) + low-Al Cpx growth zone (Fig. 8c). The increasing width of the kink with the proportion of Grt(II) (from ~100 μm in Fig. 5d to ~200 μm in Fig. 5e) may suggest that the kinking promotes Grt(II) growth which further hardens the microstructure leading to an increase in misorientation (Fig. 8). Away from the deformed regions, the Cpx is dense with chlorite (~30%) forming along cleavage planes. The cleavages are visibly displaced where the Grt(II) + Al-poor Cpx is best developed, giving a sense of shear as shown in Fig. 5d, e. The replacement of an Al-rich Cpx by a Grt and a new Cpx has already been described in the region by Griffin (1972) and Austrheim and Griffin (1985). Similar to our case, the Grt is almandine rich and the Cpx has a low Na content (3–4 wt%). Using classical thermobarometry, they interpreted this assemblage as reflecting eclogite facies condition. This alternative scenario is also in agreement with our estimation (Fig. 11b).

While interpretation of the temporal development of microstructure is equivocal, the textures in Figs. 5 and 6 indicate that variations in local stress exist within the Cpx, and that the build-up of the stress and the fluid-induced reactions are broadly contemporaneous. The formation of the array of kinks would produce zones of compression and dilation within the Cpx, the zones of compression first indicated by the white bands in Fig. 5a. No Chl forms along these bands but is able to form within the dilated cleavages. As deformation continues the shear bands develop into visible kinks, deforming the cleavage planes and associated chlorite (Fig. 5e), and ultimately becoming the sites for reaction to Grt(II) + Al-poor Cpx. The increase in the proportion of Grt (II) in the sheared zones increases with the measured displacement of the cleavages across the kink from ~34 μm in Fig. 5d to ~71 μm in Fig. 5e.

Determining an exact chronology of events may not be possible in such an evolving system especially as there would be some feedback between the deformation and fluid infiltration. However, while it may not be possible to determine the temporal relationship between the development of the Grt(II) + low-Al Cpx in the fractures and the growth of Chl in the cleavages, both reactions replace the original Al-rich Cpx crystal and are evaluated in terms of mass balances in the next section.

An alternative interpretation could be that the kinks described here represent healed fractures where fluid infiltration initiated the local reaction of Al-rich Cpx to Grt(II) + low-Al Cpx. The low-angle deformation zone around these fractures could then be the result of dislocation climb and recovery forming a network of sub-grain boundaries. The reaction to form Chl could be a later fluid infiltration event with the reaction taking place along the already-kinked cleavage planes.

However, the spatial distribution and progressive development of the Grt(II) + low-Al Cpx in regions of higher strain, and the absence of Chl in these regions is a significant observation and may indicate that the local stress regime was a controlling factor in the reactions.

5.1. Mass balance calculations

Mass balance calculations provide an important clue to understanding element transfer and mobility in fluid-induced reactions (Centrella et al., 2015, 2016; Gresens, 1967). To determine how the mass evolves

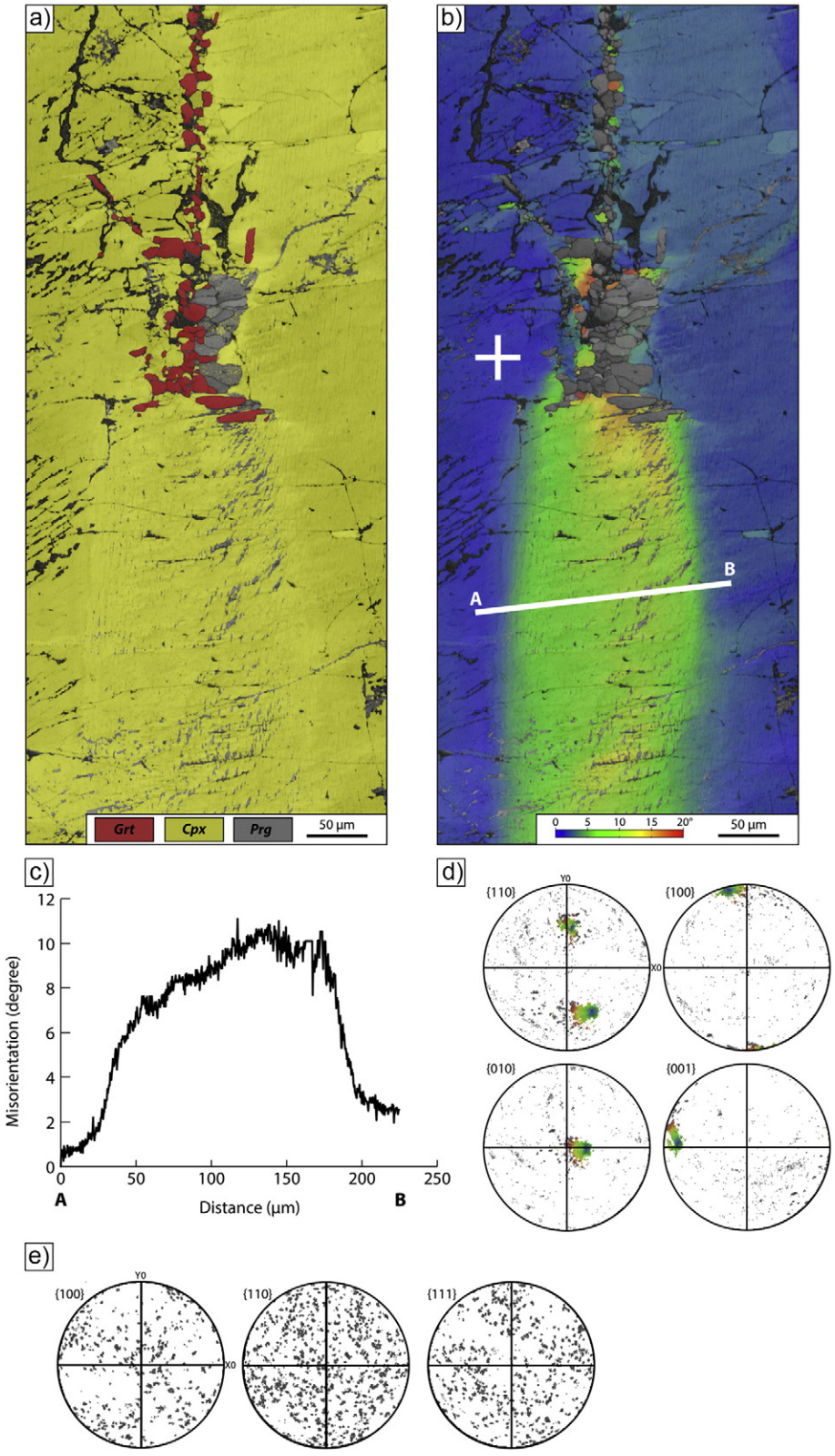

Fig. 10. EBSD data from Cpx at the tip of the new generation of Grt. a) Phase map overlain with band contrast. b) Texture map overlain with band contrast. Step size of the maps was 0.35 µm. c) Misorientation profile of the white line drawn in (b). Reference crystal is represented by the white cross in (a). d) Lower hemisphere equal area projection showing the Cpx crystal orientations (1,376,490 data points). Colours in the map b) and the pole figures d) are correlated. e) Lower hemisphere equal area projection showing the Grt crystal orientations (33,686 data points).

within any reaction volume, it is necessary to estimate the local density of this volume, including all the phases present. For the reaction from Al-rich Cpx to Grt(II) + low-Al Cpx the densities of each phase were determined from the linear combination of end-members, assuming ideal solid solution. Although there is a difference between assuming that linear mixing on molar volumes is not the same as density, our

Table 2
Table representing the local bulk composition of the Al-rich Cpx, Grt(II) + low-Al Cpx and Chl with respective densities.

	Al-rich Cpx	Grt(II) + low-Al Cpx	Chl
Density	3.5	3.6	2.6
SiO_2	48.58	46.04	30.97
TiO_2	0.04	0.08	0.01
Al_2O_3	11.71	12.02	16.83
Cr_2O_3	0.01	0.01	0.01
FeO	6.27	13.12	16.08
MnO	0.03	0.16	0.05
MgO	10.62	11.49	21.83
CaO	19.83	15.51	0.42
Na_2O	2.13	0.90	0.06
K_2O	0.01	0.02	0.02
Totals	99.23	99.35	86.28

approximation yields <1% difference from thermodynamically computed density. Densities of each end-member were obtained from the database in the website of Barthelmy: http://webmineral.com/.

For the Grt(II) the estimated density was calculated from the components 41% almandine, 32% pyrope, 21% grossular, 5% andradite and 1% spessartine (Table 1). Using Eq. (1) below gives a density of Grt(II) of 3.92 $g \cdot cm^{-3}$.

$$\text{density Grt(II)} = (\text{density}_{Alm} \times X_{Alm}) + \left(\text{density}_{Prp} \times X_{Prp}\right) + \times \left(\text{density}_{Grs} \times X_{Grs}\right) + \left(\text{density}_{Adr} \times X_{Adr}\right) + \left(\text{density}_{Sps} \times X_{Sps}\right) \quad (1)$$

where $\text{density}_{Alm} = 4.32$, $\text{density}_{Prp} = 3.56$, $\text{density}_{Grs} = 3.59$, $\text{density}_{Adr} = 3.86$ and $\text{density}_{Sps} = 4.19$.

We estimate the density of Al-rich Cpx as 3.49 $g \cdot cm^{-3}$, based on a linear combination between hedenbergite-acmite-jadeite-diopside and Ca-Tschermark end-members. The data for these 5 end-members are available in the program XMapTools (Lanari et al., 2014). Chlorite has a density of 2.6 $g \cdot cm^{-3}$ based on a linear combination of Mg-Fe amesite-clinochlore-daphnite and sudoite. Using this data, it is possible to construct a density map for all phases from quantitative microprobe maps. Fig. 12a represents the density map calculated from the compositional maps using the method described above and the program XMapTools. The original Al-rich Cpx and the new low-Al Cpx both have a high diopside end-member component (Fig. 6g) and so the density between these two Cpx phases does not change significantly. However the low-Al Cpx together with Grt(II) makes the core of the kink denser than the Al-rich Cpx matrix.

The average densities of three different domains around the kink are derived from Fig. 12a and sketched in Fig. 12b. Compared to the parent Al-rich Cpx the central part of the kink composed of Grt(II) + low-Al Cpx is denser by ~2.9% while the domain of Al-rich Cpx + Chl is less dense by ~5.7%. These density changes require a redistribution of elements within the Al-rich Cpx crystal and the observation that these reactions are related to the amphibolisation event suggests redistribution through the fluid phase.

By coupling the density maps computed from microprobe chemical maps with the mass balance equation of Gresens (1967), it is possible to see locally (on a micron to millimetre scale) gains or losses of each element associated with a reaction. In a Gresens analysis it is necessary to determine the relationship between the compositional changes and the volume changes associated with any reaction, and hence the densities of the phases involved must also be known. Note that in a commonly-used simplification of Gresens analysis (Grant, 1986, 2005) termed isocon analysis, gains and losses of elements are calculated on the assumption that at least one element is immobile and that volume and density is preserved. The Gresens equation allows the system to be open for all components to be mobile and determines gains and losses of each component relative to the unaltered mineral or rock as a function of the volume change (volume factor) for the reaction. This then needs to be combined with either microstructural observations or other evidence of specific element transport to determine the most likely combination of volume change and mass transfer. Here we are interested in the volume changes for the reaction to Grt(II) + low-Al Cpx and for the reaction to form Chl, both compared to the parent Al-rich Cpx. The composition of the Al-rich Cpx, the Chl and the Grt(II) + low-Al Cpx with their respective densities are shown in Table 2. The bulk composition for the domains Grt(II) + low-Al Cpx and for the Chl were obtained by selecting polygonal surfaces and extracting

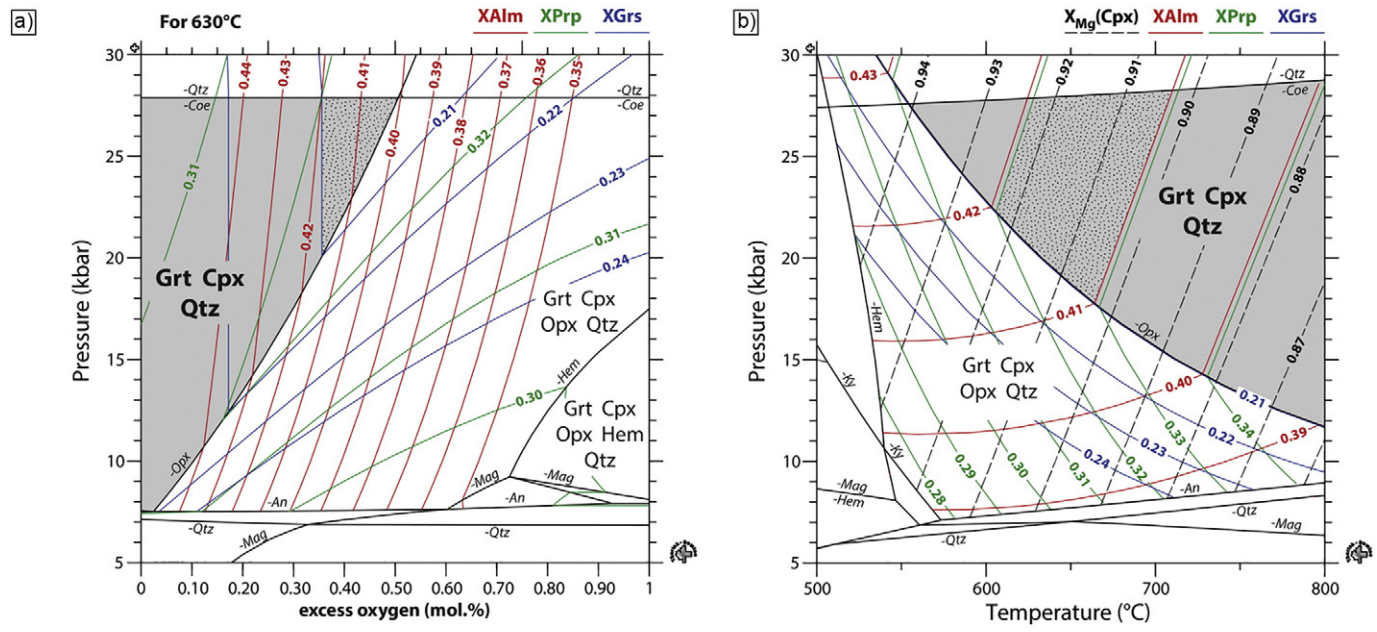

Fig. 11. a) P-X diagram using the bulk composition of the assemblage Grt(II) + low-Al Cpx, Si(43.88)Al(13.50)Fe(10.46)Mg(16.32)Ca(15.84)H(0)O(?), to estimate the excess of oxygen at 630 °C. For more visibility, the isopleths are not all represented. The assemblage field is represented in light grey and the range of possible excess of oxygen in the dotted field. b) P-T pseudosections using the bulk composition of the assemblage Grt(II) + low-Al Cpx, Si(43.88)Al(13.50)Fe(10.46)Mg(16.32)Ca(15.84)H(0)O(?)O(0.36). For more visibility, the isopleths are not all represented. The assemblage field is represented in light grey and the peak condition in the dotted field.

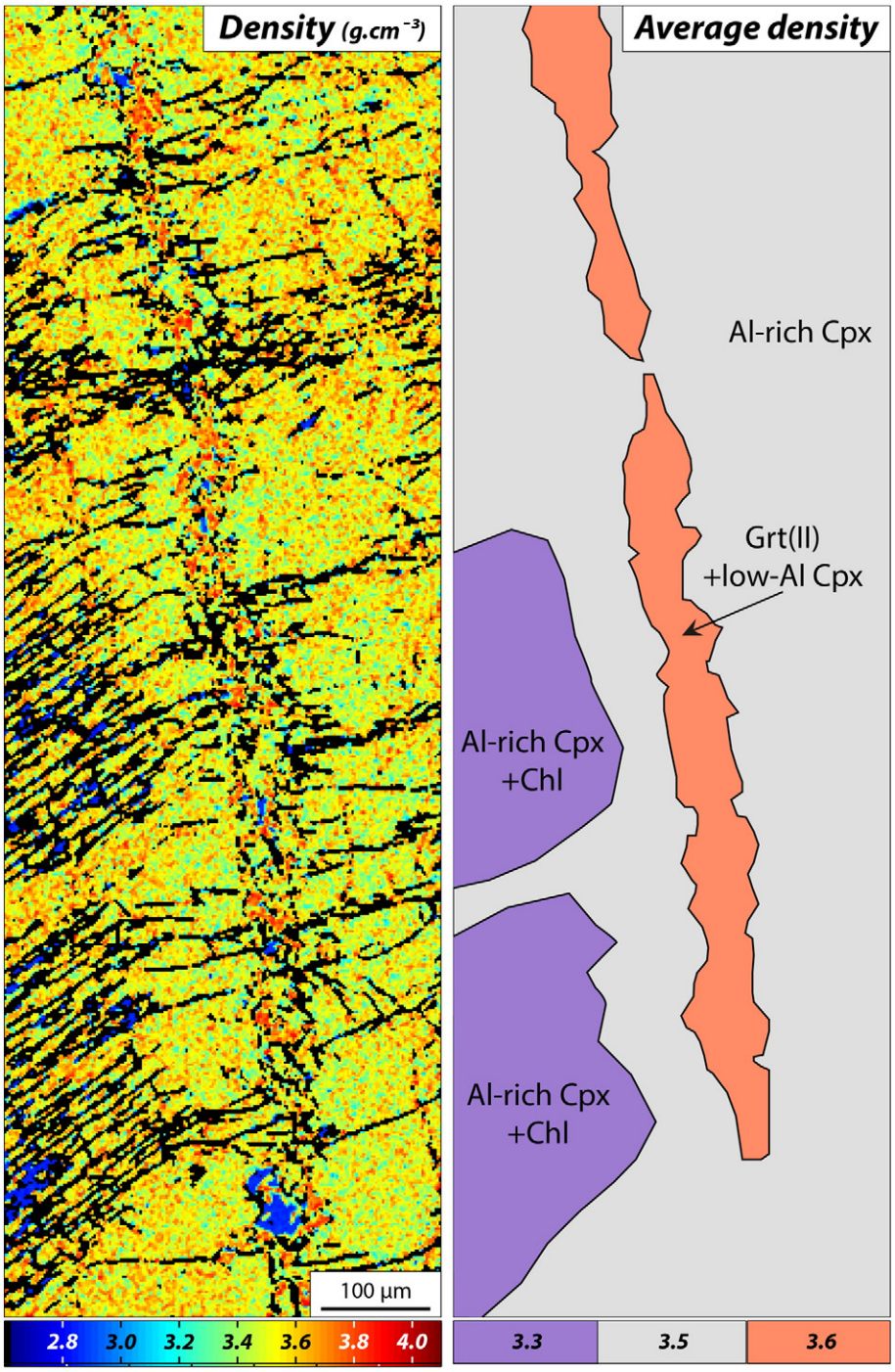

Fig. 12. a) Density map obtained with XMapTools v. 2.2.1 (Lanari et al., 2014). b) Average densities for different domains: Al-rich Cpx (grey), Grt(II) + low-Al Cpx (orange) and Al-rich Cpx + Chl (blue).

the corresponding local bulk composition using XMapTools (Mészáros et al., 2016).

From the Gresens equation, composition-volume diagrams show the gains and losses of each component in a reaction as a function of the volume factor for the reaction (Gresens, 1967). In an open system a wide range of possible balanced equations is possible, each associated with different element gains and losses and volume factors. These are shown as linear plots for several major elements in Fig. 13a. The zero gain-loss line defines reactions where specific elements are immobile. For example, if Al was immobile for the reaction of Al-rich Cpx to Grt(II) + low-Al Cpx, the volume factor would be 0.94 and the reaction would involve a loss of SiO_2 and CaO to the fluid and gains in MgO and FeO. On the other hand if SiO_2 was immobile the volume factor would be 1.03 and the reaction would involve a loss of CaO and a net gain of the other plotted elements. This is equivalent to a range between a volume loss of 6% and a volume gain of 3%.

The equivalent plot for the replacement of the parent Al-rich Cpx by Chl can take place over a wide range of volume factors between 0.96 and 2.1 (Fig. 13a) depending on whether Al or Si is considered to be immobile respectively. This means that the formation of Chl induces either

a volume loss of up to 4% or gains up to 110% in volume. The gains and losses in volume in Fig. 13a are relative to the volume of 100 g of parent Al-rich Cpx.

Fig. 13b represents the mass gains and losses of components for these two reactions compared to the parent Al-rich Cpx over the respective range of volume factors. For both reactions the mass gains and losses are consistent and behave in the same way compared to the parent Al-rich Cpx: FeO, Al_2O_3, MnO and MgO are gained whereas SiO_2, CaO and Na_2O are lost. The percentages represent the values of mass gained and lost compared to the parent Al-rich Cpx composition. The error bars represent the maximum mass values gained or lost for the range of different volumes of reaction defined by the Gresens equation (see Fig. 13a). Both reactions, to Grt(II) + low-Al Cpx and to Chl, involve a mass loss of CaO up to 21% and 98% respectively. The first assemblage contains around 15 wt% of CaO whereas Chl does not contain Ca (Table 2). During the replacement of Al-rich Cpx by Chl, Ca is released into the fluid allowing calcic phases

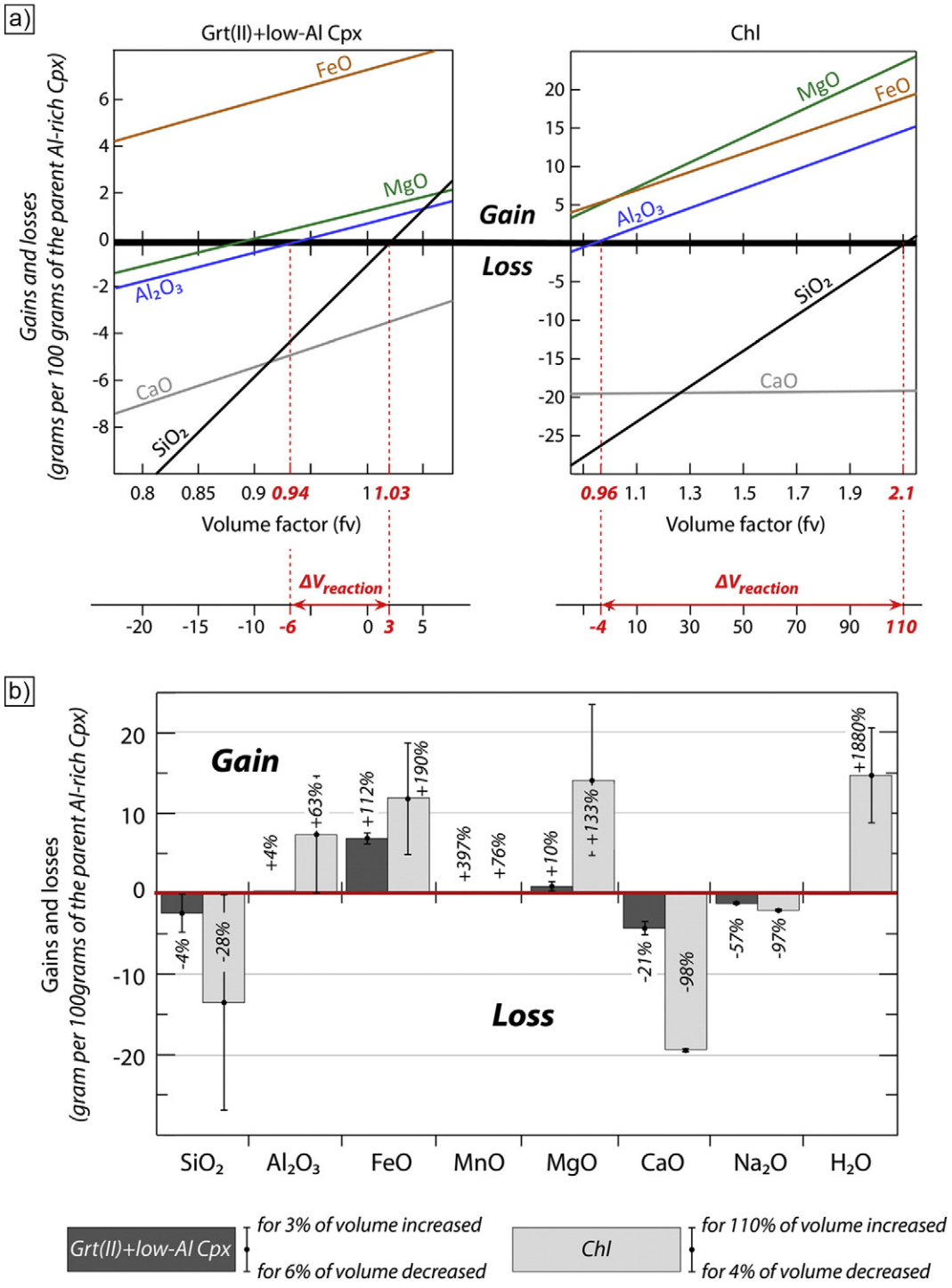

Fig. 13. a) The overall gains and losses of elements from the replacement of Al-rich Cpx by Grt(II) + low-Al Cpx and Al-rich Cpx by Chl during the hydration of the granulite, calculated from quantitative microprobe maps coupled with the Gresens analysis. b) The overall gains and losses for both reactions within the available range of volume factors. TiO_2, Cr_2O_3 and K_2O are missing because their concentrations are below the detection limit of the microprobe.

such as calcite and titanite to be formed (Fig. 5f).Their association with Chl in the cleavage planes suggests the coupling with the replacement of Chl. Note that for the replacement of Al-rich Cpx by Chl, the error bars for SiO_2 and CaO represent a maximum of loss because only a small amount of titanite and calcite is present but is not included in the analysis. The formation of these two phases indicates the presence of CO_2 within the infiltrating fluid (Markl and Piazolo, 1999), consistent with the composition of CO_2-rich (~95%) fluid inclusion found in the amphibolite facies shear zones (Andersen et al., 1991).

For all the major elements plotted in Fig. 13b the mass transfer behaves in the same way for the two different reactions within the respective range of volume factor. This can be expressed in terms of the mass balances for both reactions, using Gresens analysis. The reaction for replacement of Al-rich Cpx by Grt(II) + low-Al Cpx, for an average volume factor of 0.97, can be written as the following equation (Eq. (2)):

$$100\text{g Al-rich Cpx} + 0.05\text{g } TiO_2 + 0.32\text{g } Al_2O_3 + 6.86\text{g FeO} + 0.13\text{g MnO} + 0.88\text{g MgO} + 0.01\text{g } K_2O = 100.18\text{g(Grt(II) + low-Al Cpx)} + 2.52\text{g } SiO_2 + 4.31\text{g CaO} + 1.22\text{g } Na_2O \quad (2)$$

This equation shows that 100 g of parent Al-rich Cpx reacts with 8.23 g of element oxides if the reaction loses 3% of volume. To simulate a perfect balance of volume between the two reactions, we assume an opposite volume factor for the formation of Chl at 1.03 (Eq. (3)). For this reaction, 100 g of parent Al-rich Cpx reacts with 13.43 g of element oxides:

$$100\text{g Al-rich Cpx} + 1.21\text{g } Al_2O_3 + 6.07\text{g FeO} + 0.01\text{g MnO} + 6.14\text{g MgO} + 0.01\text{g } K_2O = 67\text{gChl} + 24.81\text{g } SiO_2 + 0.03\text{g } TiO_2 + 19.51\text{g CaO} + 2.08\text{g } Na_2O \quad (3)$$

Although the two reactions are different in terms of paragenesis, density and volume, the elements gained and lost as well as the total amount of mass require for each reaction are very similar. Although this may be coincidental, it implies a similar fluid composition input and output and suggests a single fluid-related event.

Over most of the plausible element exchange scenarios the Chl-forming reaction involves a local increase in volume, whereas the increased density for the Grt(II) + low-Al Cpx reaction involves a decrease in volume. These density changes would in turn generate local stresses within the crystal, possibly resulting in fracturing and opening the cleavage planes for further fluid infiltration and chlorite growth. Using thermodynamic arguments, Wheeler (1987) has suggested that the differential stress produced by hydration reactions can also contribute to deformation processes. Based on microstructures and calculated stresses, the local stress produced by reactions that consume fluid can be up to a few hundred MPa (Jamtveit et al., 2000, 2008, 2009; Jamtveit and Hammer, 2012; Kelemen and Hirth, 2012; Wheeler, 2014, 2015a, 2015b). In this context, we suggest the possibility that the stress generated by the formation of Chl might be locally compensated by the formation of Grt(II) + low-Al Cpx and by the mass transfer through the fluid phase and that variations in local stress may play a role in determining the reactions that take place.

5.2. Local stress variations

The consequences of local volume changes due to fluid–mineral reactions are being actively explored in relation to potential offsets of metamorphic reactions due to the generation of local stresses dependent on specific fluid pathways (Wheeler, 2014). As a function of the pathways of the fluid, the differential stresses may produce assemblages that would otherwise be interpreted as higher or lower pressure than the actual pressure. Although the details of the model are currently under discussion (Fletcher, 2015; Hobbs and Ord, 2015; Schmalholz et al., 2014; Wheeler, 2015a) there is increasing evidence that volume changes associated with metamorphic reactions and the resultant grain-scale pressure variations may determine which reactions take place in a system that is also externally stressed (Tajčmanová, 2015; Tajčmanová et al., 2014; Wintsch and Andrews, 1988).

The variation of stresses in the Al-rich Cpx, demonstrated by the variations in strain measured by misorientation in the EBSD maps, could be implicated in the reactions described here. The reaction of Al-rich Cpx to Grt(II) + low-Al Cpx is located in kinks related to a local variation of stress and strain and the reaction generates a local volume decrease i.e. a local compression. Chlorite does not form along the kinks containing Grt(II) where the compressional stresses are highest and the volume increase in forming chlorite suggests local dilatational areas. This could indicate that the distribution of fluid in the rock might be controlled by the local stress distribution, knowing that fluids are driven by fluid-pressure gradients.

A similar conclusion was reached by Mukai et al. (2014) who described a garnet in an amphibolitised granulite, where one side of the garnet was replaced by quartz + kyanite while the other side, along a fluid-rich pathway was being replaced by chlorite and amphibole.

Pargasite (Prg) is only rarely found but is present at the tip of the fracture as well as in the plume of deformed material ahead of the fracture tip in Figs. 7 and 10. The presence of the Na-bearing amphibole clearly suggests the presence of a fluid phase with the Na possibly coming from the reaction to form Grt(II) + low-Al Cpx (Eq. (2)).

5.3. Modelling of phase equilibria

Irrespective of whether the reactions described above are contemporaneous or not, it is nevertheless instructive to consider under what conditions the Al-rich Cpx would react to form Grt(II) + low-Al Cpx. This also raises the issue of whether such equilibrium calculations are appropriate. If the reactions to Grt(II) + low-Al Cpx and to Chl took place at different times, a conventional P,T estimation might indicate a P,T path for the rock. On the other hand, if the reactions were contemporaneous, can local equilibrium be assumed as argued by Vrijmoed and Podladchikov (2015) despite the fact that the system as a whole is undergoing hydration, retrograde reactions and is out of equilibrium (Jamtveit et al., 2016).

Since the reactions took place in the part of the rock that was hydrated at amphibolite-facies conditions (Fig. 2) with the presence of hydrous phases such as amphiboles, epidotes and chlorite, we consider how the addition of water affects the stability field of the Grt + low-Al Cpx assemblage. The presence of calcite and titanite associated to Chl suggests the presence of CO_2 in the fluid phase. We used the local bulk composition of the assemblage Grt(II) + low-Al Cpx (Table 2) with a significant amount of H_2O in the system (5 mol%) but we reduced its activity to 0.25 to simulate the presence of CO_2 in the fluid (Andersen et al., 1991). The corresponding hydrous isochemical equilibrium phase diagram is presented in Fig. 14. The relevant field is shown in light grey by the assemblage Grt-Cpx-Qtz-H_2O (in bold). As in the previous model presented in Fig. 11, Qtz is predicted but represents <3% of the calculated assemblage. Using the Grt(II) isopleths to constrain the P-T conditions ($Alm_{41}Prp_{32}Grs_{21}$) and the X_{Mg} of Cpx (~0.91), the assemblage is stable between 17 and 28 kbar and between 620 and 730 °C (dotted field). The P-T conditions do not change from the anhydrous model (Fig. 11) even by adding water with a low activity into the system. Although not shown here this conclusion remains unchanged when the water activity is even lower ($a_{H2O} = 0.05$).

The hydration shown in Fig. 2 takes place at amphibolite facies conditions and the determined pressure estimate gave a maximum of 12 kbar (Boundy et al., 1996). The specific mass transfer involved in the formation of the two assemblages Grt(II) + low-Al Cpx and Chl (Fig. 13b) may indicate that the deformation and associated fluid-induced reactions are related to the same event and neither of these reactions takes place in the unhydrated granulite part of the sample (Fig. 1b). The presence of fluid with a low water activity, supported by

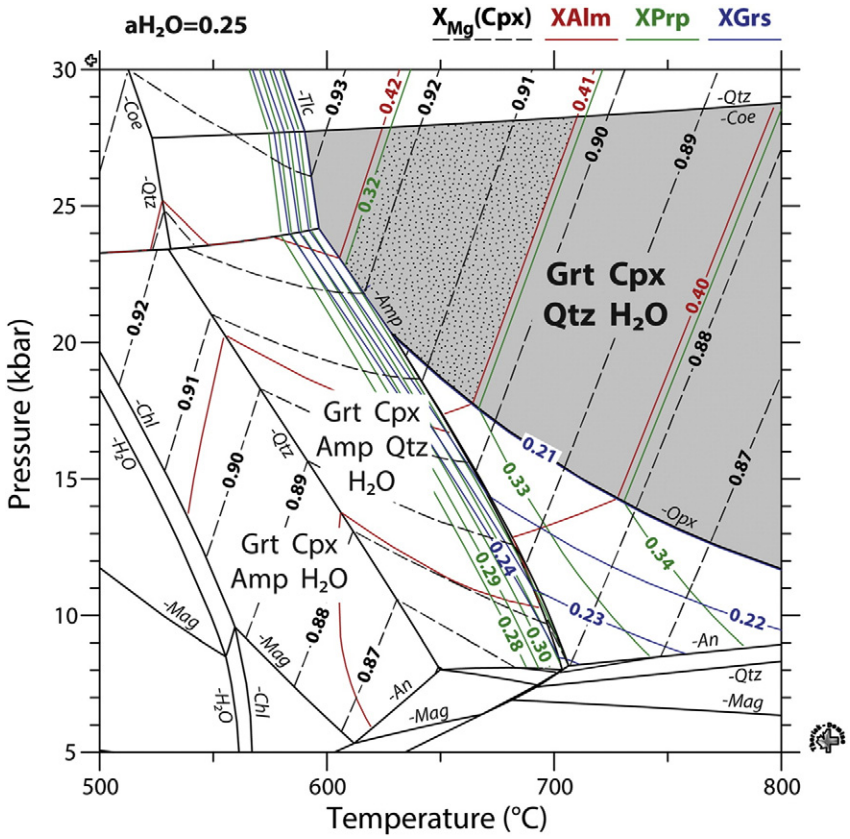

Fig. 14. P-T pseudosections using the bulk composition of the assemblage Grt(II) + low-Al Cpx, Si(43.88)Al(13.50)Fe(10.46)Mg(16.32)Ca(15.84)H(5)O(?)O(0.36) with $a_{H2O} = 0.25$. For more visibility, the isopleths are not all represented. The assemblage field is represented in light grey and the peak condition in the domain with black dots.

the presence of Ttn and Cal, doesn't influence the P-T conditions of the assemblage Grt(II) + low-Al Cpx. However, the equilibrium pressure calculated for this reaction is at least 6 kbar higher than that determined for the whole rock (Andersen et al., 1991; Boundy et al., 1996).

We can now consider a number of possible interpretations of the textural and compositional data and the modelling:

1. The first interpretation could be that the reaction of the Al-rich Cpx to Grt(II) + low-Al Cpx is not contemporaneous with the formation of Chl in the same crystal. The formation of Grt(II) + low-Al Cpx in kinks could represent healed fractures and deformation which predate the fluid event that formed the Chl. The high pressure stability for this reaction could then indicate an eclogite facies metamorphic event that is overprinted by an amphibolite metamorphism during subsequent uplift. The presence of an eclogite facies overprinting granulite has been well-documented in the Bergen Arcs (Austrheim, 1987; Bingen et al., 2004; Jamtveit et al., 1990). However the superposition of two such events in the same hand specimen is difficult to reconcile with the lack of any evidence for an eclogite facies event elsewhere in the rock and the fact that the hydration event is defined spatially by the sharp interface with the unreacted dry granulite. The two reactions described in this paper only occur in the hydrated part of the sample. The fact that both the amphibolite and eclogite facies metamorphism depend on hydration would then require that two hydration events, widely separated in time and depth in the crust, were both defined by this single hydration interface. This seems an unlikely situation.
2. The other alternative is that the reactions are broadly contemporaneous and associated with a single hydration event. This raises the immediate problem of how to interpret the pressure difference of between 6 and 13 kbar between the modelled reaction to Grt(II) + low-Al Cpx and the pressure calculated for the amphibolite facies whole rock. Such pressure values are very similar to those predicted by Tajčmanová et al. (2014), Wheeler (2014), Tajčmanová (2015). On the other hand, it may not be appropriate to use thermodynamic modelling for a hydration event that at least starts out far from equilibrium. However, arguments for local-scale equilibrium have been advanced by Evans et al. (2013) and Vrijmoed and Podladchikov (2015) even for situations where on a large scale the system is out of equilibrium, as discussed by Jamtveit et al. (2016).

On balance, we consider that the evidence presented here favours the second of these two interpretations, and that the rocks in the Bergen Arcs provide a suitable environment where the role of deformation, fluid infiltration and both grain-scale and field-scale pressure variations can be related to metamorphic reactions. Microstructural observations such as those made in this paper contribute to the debate, made largely through thermomechanical numerical simulations (Gerya, 2015; Reuber et al., 2016; Schmalholz et al., 2014; Schmalholz and Podladchikov, 2013, 2014) on the magnitudes and effects of non lithostatic pressure on the depth at which high pressure metamorphism takes place.

6. Conclusions

The textural evidence indicates that the reaction from Al-rich pyroxene to garnet + Al-poor pyroxene in some parts of the crystal and to chlorite in others is broadly contemporaneous. P-T estimates indicate a pressure difference of between 6 and 13 kbar between the reaction in the kink and that estimated for the whole rock. Whether such large pressure gradients are real or whether it is inappropriate to model phase equilibria in a non-equilibrium situation, where local differences

in the stress and availability of fluid may control reactions, is an open question.

Our conclusion takes the form of a hypothesis. In a rock or mineral where large stress gradients exist, retrograde hydration reactions taking place far from equilibrium may be influenced by factors other than the prevailing P-T conditions. We hypothesise that reactions may be driven by the tendency to reduce strain gradients associated to the kink banding by compensating positive volume changes with the formation of Chl in some areas by negative volume changes in other areas with the formation of the assemblage Grt(II) + low-Al Cpx. Our observation that a volume reducing reaction from high-Al Cpx to Grt(II) + low-Al Cpx takes place in domains of high stress and strain around kinks banding while the volume increasing replacement of high-Al Cpx by chlorite takes place in regions of low stress and strain is broadly consistent with such an hypothesis. The reactions described here are induced by the overall hydration of the rock and it is likely that the redistribution of elements that will take place in a stress gradient is enhanced by mobility through a fluid phase.

Supplementary data to this article can be found online at https://doi.org/10.1016/j.lithos.2017.11.002.

Acknowledgement

This work is supported through the EU Initial Training Network "Flowtrans" Contract No. 316889 and by ARC Grant DP160103449 to AP. We thank Steve Reddy for help with collecting the EBSD data and the valuable comments and corrections suggested on an earlier version of the manuscript. We acknowledge helpful discussions with several colleagues including Andreas Beinlich, Bjørn Jamtveit and Olivier Galland. We thank Evangelos Moulas and Alasdair Skelton for their interesting and helpful reviews.

References

Ague, J.J., 1991. Evidence for major mass transfer and volume strain during regional metamorphism of pelites. Geology 19, 855–858.
Ague, J.J., 1994. Mass transfer during Barrovian metamorphism of pelites, south–central Connecticut. 1. Evidence for changes in composition and volume. American Journal of Science 294, 989–1057.
Andersen, T., Austrheim, H., Burke, E., 1991. Fluid-induced retrogression of granulites in the Bergen Arcs, Caledonides of W. Norway: fluid inclusion evidence from amphibolite-facies shear zones. Lithos 27 (1):29–42. https://doi.org/10.1016/0024-4937(91)90018-G.
Austrheim, H., 1987. Eclogitization of lower crustal granulites by fluid migration through shear zones. Earth and Planetary Science Letters 81 (2–3):221–232. https://doi.org/10.1016/0012-821X(87)90158-0.
Austrheim, H., 2013. Fluid and deformation induced metamorphic processes around Moho beneath continent collision zones: examples from the exposed root zone of the Caledonian mountain belt, W-Norway. Tectonophysics 609:620–635. https://doi.org/10.1016/j.tecto.2013.08.030.
Austrheim, H., Boundy, M., 1994. Pseudotachylytes generated during seismic faulting and eclogitization of the deep crust. Science (New York, N.Y.) 265.
Austrheim, H., Griffin, W.L., 1985. Shear deformation and eclogite formation within granulite-facies anorthosites of the Bergen Arcs, western Norway. Chemical Geology 50 (1–3):267–281. https://doi.org/10.1016/0009-2541(85)90124-X.
Baldwin, J.A., Powell, R., Brown, M., Moraes, R., Fuck, R.A., 2005. Modelling of mineral equilibria in ultrahigh-temperature metamorphic rocks from the Anápolis-Itauçu Complex, central Brazil. Journal of Metamorphic Geology 23 (7):511–531. https://doi.org/10.1111/j.1525-1314.2005.00591.x.
Barthelmy, D., d. Mineralogy databasehttp://webmineral.com/.
Beach, A., Fyfe, W.S., 1972. Contributions to Mineralogy and Petrology 175–180 (1972).
Bingen, B., Davis, W.J., Austrheim, H., 2001. Zircon U-Pb geochronology in the Bergen arc eclogites and their Proterozoic protoliths, and implications for the pre-Scandian evolution of the Caledonides in western Norway. Geologic Society of America 113 (5), 640–649.
Bingen, B., Austrheim, H., Whitehouse, M.J., Davis, W.J., 2004. Trace element signature and U–Pb geochronology of eclogite-facies zircon, Bergen Arcs, Caledonides of W Norway. Contributions to Mineralogy and Petrology 147 (6):671–683. https://doi.org/10.1007/s00410-004-0585-z.
Boundy, T.M., Fountain, D.M., Austrheim, H., 1992. Structural development and petrofabrics of eclogite facies shear zones, Bergen Arcs, western Norway: implications for deep crustal deformational processes. Journal of Metamorphic Geology 10, 127–146.
Boundy, T.M., Essene, E.J., Hall, C.M., Austrheim, H., Halliday, A.N., 1996. Rapid exhumation of lower crust during continent-continent collision and late extension: evidence from $^{40}Ar/^{39}Ar$ incremental heating of hornblendes and muscovites, Caledonian orogen, western Norway. Geologic Society of America 108 (9), 1425–1437.
Brace, W.F., Ernst, W.G., Wittels Kallberg, R., 1970. An experimental study of tectonic overpressure in Franciscan rocks. Geological Society of America Bulletin 81, 1325–1338.
de Bresser, J., Ter Heege, J., Spiers, C., 2001. Grain size reduction by dynamic recrystallization: can it result in major rheological weakening? International Journal of Earth Sciences 90 (1):28–45. https://doi.org/10.1007/s005310000149.
Burov, E., Jolivet, L., Le Pourhiet, L., Poliakov, A., 2001. A thermomechanical model of exhumation of high pressure (HP) and ultra-high pressure (UHP) metamorphic rocks in Alpine-type collision belts. Tectonophysics 342 (1–2):113–136. https://doi.org/10.1016/S0040-1951(01)00158-5.
Camacho, A., Lee, J.K.W., Hensen, B.J., Braun, J., 2005. Short-lived orogenic cycles and the eclogitization of cold crust by spasmodic hot fluids. Nature 435 (7046):1191–1196. https://doi.org/10.1038/nature03643.
de Capitani, C., Petrakakis, K., 2010. The computation of equilibrium assemblage diagrams with Theriak/Domino software. American Mineralogist 95 (7):1006–1016. https://doi.org/10.2138/am.2010.3354.
Carmichael, D.M., 1969. On the mechanism of prograde metamorphic reactions in quartz-bearing pelitic rocks. Contributions to Mineralogy and Petrology 20 (20), 244–267.
Centrella, S., Austrheim, H., Putnis, A., 2015. Coupled mass transfer through a fluid phase and volume preservation during the hydration of granulite: an example from the Bergen Arcs, Norway. Lithos 236–237:245–255. https://doi.org/10.1016/j.lithos.2015.09.010.
Centrella, S., Austrheim, H., Putnis, A., 2016. Mass transfer and trace element redistribution during hydration of granulites in the Bergen Arcs, Norway. Lithos 262:1–10. https://doi.org/10.1016/j.lithos.2016.06.019.
Coggon, R., Holland, T.J.B., 2002. Mixing properties of phengitic micas and revised garnet-phengite thermobarometers. Journal of Metamorphic Geology 20 (7):683–696. https://doi.org/10.1046/j.1525-1314.2002.00395.x.
Cohen, A.S., O'Nions, R.K., Siegenthaler, Siegenthaler, R., Griffin, W.L., 1988. Chronology of the pressure-temperature history recorded by a granulite terrain. Contributions to Mineralogy and Petrology 98, 303–311.
Diener, J.F.A., Powell, R., White, R.W., Holland, T.J.B., 2007. A new thermodynamic model for clino- and orthoamphiboles in the system Na_2O-CaO-FeO-MgO-Al_2O_3-SiO_2-H_2O-O. Journal of Metamorphic Geology 25 (6):631–656. https://doi.org/10.1111/j.1525-1314.2007.00720.x.
Erambert, M., Austrheim, H., 1993. The effect of fluid and deformation on zoning and inclusion patterns in poly-metamorphic garnets. Contributions to Mineralogy and Petrology 115 (2):204–214. https://doi.org/10.1007/BF00321220.
Evans, K.A., Powell, R., Frost, B.R., 2013. Using equilibrium thermodynamics in the study of metasomatic alteration, illustrated by an application to serpentinites. Lithos 168–169:67–84. https://doi.org/10.1016/j.lithos.2013.01.016.
Fitz Gerald, J.D., Stünitz, H., 1993. Deformation of granitoids at low metamorphic grade. I: reactions and grain size reduction. Tectonophysics 221, 269–297.
Fletcher, C.R., 2015. Dramatic effects of stress on metamorphic reactions. Geology 255, e354. https://doi.org/10.1130/G36302C.1.
Fukuda, J.I., Okudaira, T., Satsukawa, T., Michibayashi, K., 2012. Solution–precipitation of K-feldspar in deformed granitoids and its relationship to the distribution of water. Tectonophysics 532–535:175–185. https://doi.org/10.1016/j.tecto.2012.01.033.
Fyfe, W.S, Price, N.J, Thompson, A.B, 1978. Fluids in the earth's crust. Elsevier, Amsterdam, p. 383.
Gerya, T., 2015. Tectonic overpressure and underpressure in lithospheric tectonics and metamorphism. Journal of Metamorphic Geology 33 (8):785–800. https://doi.org/10.1111/jmg.12144.
Glodny, J., Kühn, A., Austrheim, H., 2008. Geochronology of fluid-induced eclogite and amphibolite facies metamorphic reactions in a subduction–collision system, Bergen Arcs, Norway. Contributions to Mineralogy and Petrology 156 (1):27–48. https://doi.org/10.1007/s00410-007-0272-y.
Grant, J.A., 1986. The isocon diagram—a simple solution to Gresens' equation for metasomatic alteration. Economic Geology 81, 1976–1982.
Grant, J.A., 2005. Isocon analysis: a brief review of the method and applications. Physics and Chemistry of the Earth, Parts A/B/C 30 (17–18):997–1004. https://doi.org/10.1016/j.pce.2004.11.003.
Gratier, J.P., Dysthe, D., Renard, F., 2013. The role of pressure solution creep in the ductility of the earth's upper crust. Archives Ouvertes 1–112.
Gresens, R.L., 1967. Composition-volume relationships of metasomatism. Chemical Geology 2:47–65. https://doi.org/10.1016/0009-2541(67)90004-6.
Griffin, W.L., 1972. Formation of eclogites and coronas in anorthosites, Bergen Arcs, Norway. Studies in Mineralogy and Precambrian Geology. vol. 135.
Griffin, W.L, Heier, K.S., 1973. Petrological implications of some corona structures. Lithos 6 (4):315–335. https://doi.org/10.1016/0024-4937(73)90051-0.
Hawthorne, F.C., Oberti, R., Harlow, G.E., Maresch, W.V., Martin, R.F., Schumacher, J.C., Welch, M.D., 2012. Nomenclature of the amphibole supergroup. American Mineralogist 97 (11–12):2031–2048. https://doi.org/10.2138/am.2012.4276.
Heidelbach, F., Post, A., Tullis, J., 2000. Crystallographic preferred orientation in albite samples deformed experimentally by dislocation and solution precipitation creep. Journal of Structural Geology 22 (11–12):1649–1661. https://doi.org/10.1016/S0191-8141(00)00072-9.
Hobbs, B., Ord, A., 2015. Dramatic effects of stress on metamorphic reactions: COMMENT. Geology 43 (11):e372. https://doi.org/10.1130/G37070C.1.
Holland, T.J.B., Powell, R., 1990. An enlarged and updated internally consistent thermodynamic dataset with uncertainties and correlations: the system K_2O–Na_2O–CaO–MgO–MnO–FeO–Fe_2O_3–Al_2O_3–TiO_2–SiO_2–C–H_2–O_2. Journal of Metamorphic Geology 8, 89–124.

Holland, T.J.B., Powell, R., 1998. An internally consistent thermodynamic data set for phases of petrological interest. Journal of Metamorphic Geology 16, 309–343.
Holland, T., Powell, R., 2003. Activity-composition relations for phases in petrological calculations: an asymmetric multicomponent formulation. Contributions to Mineralogy and Petrology 145 (4):492–501. https://doi.org/10.1007/s00410-003-0464-z.
Holland, T.J.B., Powell, R., 2006. Mineral activity? Composition relations and petrological calculations involving cation equipartition in multisite minerals: a logical inconsistency. Journal of Metamorphic Geology 24:851–861. https://doi.org/10.1111/j.1525-1314.2006.00672.x.
Holyoke, C.W., Tullis, J., 2006. The interaction between reaction and deformation: an experimental study using a biotite + plagioclase + quartz gneiss. Journal of Metamorphic Geology 24 (8):743–762. https://doi.org/10.1111/j.1525-1314.2006.00666.x.
Jamtveit, B., Hammer, Ø., 2012. Sculpting of rocks by reactive fluids. Geochemical Perspectives 1 (3):341–481. https://doi.org/10.7185/geochempersp.1.3.
Jamtveit, B., Bucher-Nurminen, K., Austrheim, H., 1990. Fluid controlled eclogitization of granulites in deep crustal shear zones, Bergen Arcs, Western Norway. Contributions to Mineralogy and Petrology 104.
Jamtveit, B., Austrheim, H., Malthe-Sørenssen, A., 2000. Accelerated hydration of the Earth's deep crust induced by stress perturbations. Nature 408, 75–78.
Jamtveit, B., Malthe-Sørenssen, A., Kostenko, O., 2008. Reaction enhanced permeability during retrogressive metamorphism. Earth and Planetary Science Letters 267 (3–4): 620–627. https://doi.org/10.1016/j.epsl.2007.12.016.
Jamtveit, B., Putnis, C.V., Malthe-Sørenssen, A., 2009. Reaction induced fracturing during replacement processes. Contributions to Mineralogy and Petrology 157 (1): 127–133. https://doi.org/10.1007/s00410-008-0324-y.
Jamtveit, B., Austrheim, H., Putnis, A., 2016. Disequilibrium metamorphism of stressed lithosphere. Earth-Science Reviews 154:1–13. https://doi.org/10.1016/j.earscirev.2015.12.002.
Jolivet, L., Faccenna, C., Goffé, B., Burov, E., Agard, P., 2003. Subduction tectonics and exhumation of high-pressure metamorphic rocks in the Mediterranean Orogens. American Journal of Science 303, 353–409.
Karato, S.I., 1988. The role of recrystallization in the preferred orientation of olivine. Physics of the Earth and Planetary Interiors 51 (1–3):107–122. https://doi.org/10.1016/0031-9201(88)90029-5.
Kelemen, P.B., Hirth, G., 2012. Reaction-driven cracking during retrograde metamorphism: olivine hydration and carbonation. Earth and Planetary Science Letters 345-348:81–89. https://doi.org/10.1016/j.epsl.2012.06.018.
Kelsey, D.E., White, R.W., Powell, R., 2005. Calculated phase equilibria in K_2O-FeO-MgO-Al_2O_3-SiO_2-H_2O for silica-undersaturated sapphirine-bearing mineral assemblages. Journal of Metamorphic Geology 23 (4):217–239. https://doi.org/10.1111/j.1525-1314.2005.00573.x.
Kretz, R., 1983. Symbols for rock-forming minerals. American Mineralogist 68, 277–279.
Lanari, P., Engi, M., 2017. Local Bulk Composition Effects on Metamorphic Mineral Assemblages. vol. 83.
Lanari, P., Vidal, O., Andrade, V., Dubacq, B., Lewin, E., Grosch, E.G., Schwartz, S., 2014. XMapTools: a MATLAB©-based program for electron microprobe X-ray image processing and geothermobarometry. Computers & Geosciences 62:227–240. https://doi.org/10.1016/j.cageo.2013.08.010.
Leake, B.E., 1978. Nomenclature of amphiboles. American Mineralogist 1023–1052.
Lund, M.G., Austrheim, H., 2003. High-pressure metamorphism and deep-crustal seismicity: evidence from contemporaneous formation of pseudotachylytes and eclogite facies coronas. Tectonophysics 372 (1–2):59–83. https://doi.org/10.1016/S0040-1951(03)00232-4.
Mahar, E.M., Baker, J.M., Powell, R., Holland, T.J.B., Howell, N., 1997. The effect of Mn on mineral stability in metapelites. Journal of Metamorphic Geology 15 (2):223–238. https://doi.org/10.1111/j.1525-1314.1997.00011.x.
Malvoisin, B., Brunet, F., Carlut, J., Rouméjon, S., Cannat, M., 2012. Serpentinization of oceanic peridotites: 2. Kinetics and processes of San Carlos olivine hydrothermal alteration. Journal of Geophysical Research - Solid Earth 117, B04102. https://doi.org/10.1029/2011JB008842.
Markl, G., Piazolo, S., 1999. Stability of high-Al titanite from low-pressure calcsilicates in light of fluid and host-rock composition. American Mineralogist 84 (1–2):37–47. https://doi.org/10.2138/am-1999-1-204.
Marsh, J.H., Johnson, S.E., Yates, M.G., West, T.J.R., D. P., 2009. Coupling of deformation and reactions during mid-crustal shear zone development: an in situ frictional-viscous transition. Journal of Metamorphic Geology 27 (8):531–553. https://doi.org/10.1111/j.1525-1314.2009.00841.x.
Menegon, L., Pennacchioni, G., Spiess, R., 2008. Dissolution-precipitation creep of K-feldspar in mid-crustal granite mylonites. Journal of Structural Geology 30 (5): 565–579. https://doi.org/10.1016/j.jsg.2008.02.001.
Mészáros, M., Hofmann, B.A., Lanari, P., Korotev, R.L., Gnos, E., Greber, N.D., Leya, I., Greenwood, R.C., Jull, A.J.T., Al-Wagdani, K., Mahjoub, A., Al-Solami, A.A., Habibullah, S.N., 2016. Petrology and geochemistry of feldspathic impact-melt breccia Abar al' Uj 012, the first lunar meteorite from Saudi Arabia. Meteoritics & Planetary Science: 1–19. https://doi.org/10.1111/maps.12693.
Morimoto, N., 1988. Nomenclature of pyroxenes. American Mineralogist 73, 1123–1133.
Moulas, E., Podladchikov, Y.Y., Aranovich, L.Y., Kostopoulos, D., 2013. The problem of depth in geology: when pressure does not translate into depth. Petrology 21 (6): 527–538. https://doi.org/10.1134/S0869591113060052.
Mukai, H., Austrheim, H., Putnis, C.V., Putnis, A., 2014. Textural evolution of plagioclase feldspar across a shear zone: implications for deformation mechanism and rock strength. Journal of Petrology 55 (8):1457–1477. https://doi.org/10.1093/petrology/egu030.
Okamoto, A., Ogasawara, Y., Ogawa, Y., Tsuchiya, N., 2011. Progress of hydration reactions in olivine–H_2O and orthopyroxenite–H_2O systems at 250 °C and vapor-saturated pressure. Chemical Geology 289:245–255. https://doi.org/10.1016/j.chemgeo.2011.08.007.
Ostapenko, G.T., 1976. Geokhimikiya 824–844 (1976).
Parsons, I., Lee, M.R., 2009. Mutual replacement reactions in alkali feldspars I: microtextures and mechanisms. Contributions to Mineralogy and Petrology 157 (5):641–661. https://doi.org/10.1007/s00410-008-0355-4.
Pearce, M.A., Wheeler, J., Prior, D.J., 2011. Relative strength of mafic and felsic rocks during amphibolite facies metamorphism and deformation. Journal of Structural Geology 33 (4):662–675. https://doi.org/10.1016/j.jsg.2011.01.002.
Philipotts, A., Ague, J., 2013. Principles of Igneous and Metamorphic Petrology. Cambridge University.
Putnis, A., Austrheim, H., 2010. Fluid-induced processes: metasomatism and metamorphism. Geofluids. https://doi.org/10.1111/j.1468-8123.2010.00285.x.
Reuber, G., Kaus, B.J., Schmalholz, S.M., White, R.W., 2016. Nonlithostatic pressure during subduction and collision and the formation of (ultra)high-pressure rocks. Geology 44 (5):343–346. https://doi.org/10.1130/G37595.1.
de Ronde, A.A., Heilbronner, R., Stünitz, H., Tullis, J., 2004. Spatial correlation of deformation and mineral reaction in experimentally deformed plagioclase–olivine aggregates. Tectonophysics 389 (1–2):93–109. https://doi.org/10.1016/j.tecto.2004.07.054.
de Ronde, A.A., Stünitz, H., Tullis, J., Heilbronner, R., 2005. Reaction-induced weakening of plagioclase–olivine composites. Tectonophysics 409 (1–4):85–106. https://doi.org/10.1016/j.tecto.2005.08.008.
Rutter, E.H., Casey, M., Burlini, L., 1994. Preferred crystallographic orientation development during the plastic and superplastic flow of calcite rocks. Journal of Structural Geology 16 (10):1431–1446. https://doi.org/10.1016/0191-8141(94)90007-8.
Schmalholz, S.M., Podladchikov, Y.Y., 2013. Tectonic overpressure in weak crustal-scale shear zones and implications for the exhumation of high-pressure rocks. Geophysical Research Letters 40 (10):1984–1988. https://doi.org/10.1002/grl.50417.
Schmalholz, S.M., Podladchikov, Y., 2014. Metamorphism under stress: the problem of relating minerals to depth. Geology 42 (8):733–734. https://doi.org/10.1130/focus0822014.1.
Schmalholz, S.M., Duretz, T., Schenker, F.L., Podladchikov, Y.Y., 2014. Kinematics and dynamics of tectonic nappes: 2-D numerical modelling and implications for high and ultra-high pressure tectonism in the Western Alps. Tectonophysics 631:160–175. https://doi.org/10.1016/j.tecto.2014.05.018.
Schneider, J., Bosch, D., Monié, P., 2008. Individualization of textural and reactional microdomains in eclogites from the Bergen Arcs (Norway): consequences for Rb/Sr and Ar/Ar radiochronometer behavior during polymetamorphism. Geochemistry, Geophysics, Geosystems 9 (12), 1–28.
Svahnberg, H., Piazolo, S., 2010. The initiation of strain localisation in plagioclase-rich rocks: insights from detailed microstructural analyses. Journal of Structural Geology 32 (10):1404–1416. https://doi.org/10.1016/j.jsg.2010.06.011.
Svahnberg, H., Piazolo, S., 2013. Interaction of chemical and physical processes during deformation at fluid-present conditions: a case study from an anorthosite–leucogabbro deformed at amphibolite facies conditions. Contributions to Mineralogy and Petrology 165 (3):543–562. https://doi.org/10.1007/s00410-012-0822-9.
Tajčmanová, L., 2015. Deviations from lithostatic pressure during metamorphism: fact or fiction? Journal of Metamorphic Geology 33 (8):783–784. https://doi.org/10.1111/jmg.12152.
Tajčmanová, L., Podladchikov, Y., Powell, R., Moulas, E., Vrijmoed, J.C., Connolly, J., 2014. Grain-scale pressure variations and chemical equilibrium in high-grade metamorphic rocks. Journal of Metamorphic Geology 32 (2):195–207. https://doi.org/10.1111/jmg.12066.
Tajčmanová, L., Vrijmoed, J., Moulas, E., 2015. Grain-scale pressure variations in metamorphic rocks: implications for the interpretation of petrographic observations. Lithos 216-217:338–351. https://doi.org/10.1016/j.lithos.2015.01.006.
Vrijmoed, J.C., Podladchikov, Y.Y., 2015. Thermodynamic equilibrium at heterogeneous pressure. Contributions to Mineralogy and Petrology 170 (1). https://doi.org/10.1007/s00410-015-1156-1.
Walker, F.D.L., Lee, M.R., Parsons, I., 1995. Micropores and micropermeable texture in alkali feldspars: geochemical and geophysical implications. Mineralogical Magazine 59, 505–534.
Wawrzenitz, N., Krohe, A., Rhede, D., Romer, R.L., 2012. Dating rock deformation with monazite: the impact of dissolution precipitation creep. Lithos 134-135:52–74. https://doi.org/10.1016/j.lithos.2011.11.025.
Wheeler, J., 1987. The significance of grain-scale stresses in the kinetics of metamorphism. Contributions to Mineralogy and Petrology 97, 397–404.
Wheeler, J., 2014. Dramatic effects of stress on metamorphic reactions. Geology 42 (8): 647–650. https://doi.org/10.1130/G35718.1.
Wheeler, J., 2015a. Dramatic effects of stress on metamorphic reactions: COMMENT. Geology 43 (1):e355. https://doi.org/10.1130/G36302C.1.
Wheeler, J., 2015b. Dramatic effects of stress on metamorphic reactions. Geology:373 https://doi.org/10.1063/1.1702656.
White, R.W., Powell, R., Holland, T.J.B., Worley, B.A., 2000. The effect of TiO_2 and Fe_2O_3 on metapelitic assemblages at greenschist and amphibolite facies conditions: mineral equilibria calculations in the system K_2O-FeO-MgO-Al_2O_3-SiO_2-H_2O-TiO_2-Fe_2O_3. Journal of Metamorphic Geology 18, 497–511.
White, R.W., Powell, R., Clarke, G.L., 2002. The interpretation of reaction textures in Ferich metapelitic granulites of the Musgrave Block, central Australia: constraints from mineral equilibria calculations in the system K_2OFeOMgO$Al_2O_3SiO_2H_2O$$TiO_2Fe_2O_3$. Journal of Metamorphic Geology 20, 41–55.

White, R.W., Powell, R., Holland, T.J.B., 2007. Progress relating to calculation of partial melting equilibria for metapelites. Journal of Metamorphic Geology 25 (5): 511–527. https://doi.org/10.1111/j.1525-1314.2007.00711.x.

Wintsch, R.P., Andrews, M.S., 1988. Deformation induced growth of sillimanite: "stress" minerals revisited. Chicago Journal 96 (2), 143–161.

Wintsch, R.P., Yeh, M.W., 2013. Oscillating brittle and viscous behavior through the earthquake cycle in the Red River Shear Zone: monitoring flips between reaction and textural softening and hardening. Tectonophysics 587:46–62. https://doi.org/10.1016/j.tecto.2012.09.019.